

THE COSMOLOGICAL IMPACT OF LUMINOUS TEV BLAZARS II: REWRITING THE THERMAL HISTORY OF THE INTERGALACTIC MEDIUM

PHILIP CHANG^{1,2}, AVERY E. BRODERICK^{1,3,4}, AND CHRISTOPH PFROMMER^{5,1}

¹ Canadian Institute for Theoretical Astrophysics, 60 St. George Street, Toronto, ON M5S 3H8, Canada; aeb@cita.utoronto.ca, pchang@cita.utoronto.ca

² Department of Physics, University of Wisconsin-Milwaukee, 1900 E. Kenwood Boulevard, Milwaukee, WI 53211, USA

³ Perimeter Institute for Theoretical Physics, 31 Caroline Street North, Waterloo, ON, N2L 2Y5, Canada

⁴ Department of Physics and Astronomy, University of Waterloo, 200 University Avenue West, Waterloo, ON, N2L 3G1, Canada

⁵ Heidelberg Institute for Theoretical Studies, Schloss-Wolfsbrunnengasse 35, D-69118 Heidelberg, Germany; christoph.pfrommer@h-its.org

Draft version November 2, 2018

ABSTRACT

The Universe is opaque to extragalactic very high-energy gamma rays (VHEGRs, $E > 100$ GeV) because they annihilate and pair produce on the extragalactic background light. The resulting ultra-relativistic pairs are commonly assumed to lose energy primarily through inverse Compton scattering of cosmic microwave background photons, reprocessing the original emission from TeV to GeV energies. In Broderick et al. (2012, Paper I of this three paper series), we argued that this is not the case; powerful plasma instabilities driven by the highly anisotropic nature of the ultra-relativistic pair distribution provide a plausible way to dissipate the kinetic energy of the TeV-generated pairs locally, heating the intergalactic medium (IGM). Here, we explore the effect of this heating upon the thermal history of the IGM. We collate the observed extragalactic VHEGR sources to determine a local VHEGR heating rate. Given the pointed nature of VHEGR observations, we estimate the correction for the various selection effects using *Fermi* observations of high and intermediate peaked BL Lacs. As the extragalactic component of the local VHEGR flux is dominated by TeV blazars, we then estimate the evolution of the TeV blazar luminosity density by tying it to the well-observed quasar luminosity density, and producing a VHEGR heating rate as a function of redshift. This heating is relatively homogeneous for $z \lesssim 4$, but there is greater spatial variation at higher redshift (order unity at $z \sim 6$) because of the reduced number of blazars that contribute to local heating. We show that this new heating process dominates photoheating in the low-redshift evolution of the IGM and calculate the effect of this heating in a one-zone model. As a consequence, the inclusion of TeV blazar heating qualitatively and quantitatively changes the structure and history of the IGM. Due to the homogeneous nature of the extragalactic background light, TeV blazars produce a uniform *volumetric* heating rate. This heating is sufficient to increase the temperature of the mean density IGM by nearly an order of magnitude, and at low densities by substantially more. It also naturally produces the inverted temperature-density relation inferred by recent observations of the high-redshift Ly α forest, a feature that is difficult to reconcile with standard reionization models. Finally, we close with a discussion on the possibility of detecting this hot low-density IGM suggested by our model either directly or indirectly via the local Ly α forest, the Comptonized cosmic microwave background, or free-free emission, but find that such measurements are currently not feasible.

Subject headings: intergalactic medium – BL Lacertae objects: general – gamma rays: general – cosmology: theory – large-scale structure of Universe

1. INTRODUCTION

The *Fermi* satellite and ground based imaging atmospheric Cerenkov telescopes such as H.E.S.S., MAGIC, and VERITAS¹ have demonstrated that the ultra-high energy Universe is teeming with energetic very high-energy gamma-ray (VHEGR, $E > 100$ GeV) sources, the extragalactic component of which mainly consists of TeV blazars with a minority population of other sources such as radio galaxies and starburst galaxies. These VHEGR observations are being used to constrain the sites and mechanisms of particle acceleration (see, e.g., Paglione et al. 1996; Domingo-Santamaría & Torres 2005; Thompson et al. 2007; Persic et al. 2008; de Cea del Pozo et al. 2009; Rephaeli et al. 2010; Lacki et al. 2010), dynamics of black hole jets (see, e.g., Jones et al. 1974; Ghisellini & Maraschi 1989; Ghisellini & Tavecchio 2008; Tavecchio & Ghisellini 2008; Ghisellini et al. 2009), and intergalactic magnetic fields

(IGMF; Neronov & Vovk 2010; Tavecchio et al. 2010, 2011; Dermer et al. 2011; Taylor et al. 2011; Dolag et al. 2011; Takahashi et al. 2012; Vovk et al. 2012).

While these objects have an interesting phenomenology, they are believed to have a minor impact upon the Universe at large, i.e., on the formation of structures and thermodynamics. Energetically this is not an unreasonable assumption, as VHEGR emission is $\sim 0.1\%$ of the radiative power of quasars. However, in this series of papers, we show that in spite of their energetic disadvantage, TeV blazars have a significant effect on structure formation and a dominant effect on thermodynamics – that is the VHEGR emission from blazars “punches” far above its energetic weight. Namely, *if* the radiation from VHEGR sources is thermalized, as we have argued is the case in Broderick et al. (2012, hereafter Paper I), the heating due to these VHEGRs dominates photoionization heating throughout the vast majority of the Universe at $z \lesssim 3$, raising the temperature of the low-density IGM by up to two orders of magnitude.

Given that the total power emitted by AGNs and stars in the UV and X-rays vastly exceeds that due to the TeV blazars, it seems counterintuitive that blazar heating dominates pho-

¹ High Energy Stereoscopic System, Major Atmospheric Gamma Imaging Cerenkov Telescope, Very Energetic Radiation Imaging Telescope Array System.

toheating. However, the UV and X-ray background heats the intergalactic medium (IGM) inefficiently after reionization, while VHEGR photons heats the IGM efficiently via plasma beam instabilities (Paper I). This difference in the heating efficiency of photoheating vs. blazar heating is due to the difference in the rate-limiting process in each. The rate of photoheating after reionization is not limited by the availability of ionizing photons, but instead by abundance of targets, and thus recombination. On the other hand, the heating of the IGM by TeV blazars does not suffer from a deficit of targets and is only limited by the total cosmic power of VHEGR sources.

We illustrate this point with the following order of magnitude estimate. First let us estimate the amount of photoheating that the IGM suffers at the present day. The recombination rate of H is of order the Hubble time at the mean density of the Universe at present. Hence, an average H atom in the IGM will recombine once over a Hubble time only to be ionized immediately by a UV photon. Using a spectral index of -1.6 for the ionizing background, which is appropriate for quasars (Furlanetto & Oh 2008), the average amount of excess energy absorbed per ionization is $\epsilon_{\text{exc}} \approx 4\text{eV}$. The fraction of the rest mass energy of all the baryons in the universe required to produce this amount of heating in the IGM is

$$f_{\text{exc}} = \frac{\epsilon_{\text{exc}}}{m_p c^2} \approx 4 \times 10^{-9} \left(\frac{\epsilon_{\text{exc}}}{4\text{eV}} \right). \quad (1)$$

Hence, only a small amount of rest mass energy is injected as thermal energy into the IGM. An equivalent statement is that the diffuse IGM is optically thin to ionization radiation.²

By comparison, the fraction of the baryon rest mass locked up in massive black holes in the Universe is $f_{\text{BH}} \approx 9 \times 10^{-5}$ and in stars is 0.06 (Fukugita & Peebles 2004). Assuming a radiative efficiency (relative to rest mass) for black holes and stars of 0.1 and 10^{-3} respectively, we find that fraction of the baryon rest mass converted to radiation in black holes and stars is $\epsilon_{\text{rad,BH}} \sim 10^{-5}$ and $\epsilon_{\text{rad,*}} \sim 6 \times 10^{-5}$, respectively.³ This is many orders of magnitude larger than what is required by Equation (1) and demonstrates an important point: *hard ionizing radiation is inefficient at heating the IGM after H and He reionization.*

In Paper I, we argued that VHEGR photons are efficiently converted into heat in the IGM via plasma instabilities. Hence, the limiting factor is the total energy density of VHEGR photons over cosmic time. To estimate this energy density, we note that the local *observed* TeV blazar luminosity density is 2.1×10^{-3} that of the local quasar luminosity density (see Section 3.1.1), after correcting for various selection effects. Assuming that the TeV blazar luminosity density tracks the quasar luminosity density over cosmic time, this implies that the fraction of baryon rest mass that is converted to VHEGR photons (and ultimately heating of the IGM) is

$$f_{\text{TeV}} = \frac{\text{TeV Blazar Luminosity Density}}{\text{Quasar Luminosity Density}} \times \epsilon_{\text{rad,BH}} = 2.1 \times 10^{-8}, \quad (2)$$

which is nearly five times that due to photoheating (i.e., Equation (1)) and demonstrates the dominance of TeV blazar heating.

² By “diffuse” IGM, we discount Lyman limit systems.

³ Here we have likely significantly overestimated the radiative efficiency of the stellar component for two reasons. First, most of the mass locked up in the stellar component is contained in low-mass stars, which are capable of converting only a small fraction of their rest mass into energy. Second, we have not accounted for the fraction of stellar radiation that is capable of ionizing the IGM.

ing. Equivalently, the greater efficiency of TeV blazar heating compared to photoheating more than makes up for its energetic disadvantage.

The physics of this heating and its cosmological consequences is the subject of this series of three papers. In Paper I, we studied the physics of VHEGR photon propagation through the Universe. As these VHEGRs propagate through the Universe, they interact with the soft photons that comprise the extragalactic background light (EBL) and produce ultra-relativistic pairs (see, e.g., Gould & Schröder 1967; Salamon & Stecker 1998; Neronov & Semikoz 2009). Typical mean free paths are between 30 Mpc and 1 Gpc, depending upon the energy of the VHEGR and redshift, i.e., the Universe is optically thick to VHEGR. The result is a ubiquitous population of ultra-relativistic pairs, with typical Lorentz factors of 10^5 – 10^7 . Previously, it has been assumed that they lose energy exclusively through inverse-Compton scattering the cosmic microwave background (CMB) and EBL, producing GeV gamma rays that form part of the EGRB (see, e.g., Narumoto & Totani 2006; Kneiske & Mannheim 2008; Inoue & Totani 2009; Venters 2010). The non-observation of this GeV gamma-rays has been used to argue for cosmologically interesting IGMFs (Neronov & Vovk 2010; Tavecchio et al. 2010, 2011; Dermer et al. 2011; Taylor et al. 2011; Dolag et al. 2011; Takahashi et al. 2012; Vovk et al. 2012).

We then presented a plausible alternative mechanism for extracting the kinetic energy of the ultra-relativistic pairs: plasma beam instabilities. Despite the extraordinarily dilute nature of this ultra-relativistic pair plasma, we found a variety of plasma instabilities which grow on timescales short in comparison to the inverse-Compton cooling time, the most important of which is the “oblique” instability (Bret et al. 2004). Via this instability, these ultra-relativistic pairs lose their kinetic energy by depositing it as heat in the IGM. Because these beams then cool well before an inverse-Compton cascade (ICC) can develop, the simplest versions of the argument used to produce limits upon the IGMF are precluded. Hence, the existence of the IGMF does not follow from the non-observation of GeV gamma rays from existing TeV blazars as previous groups have argued. In addition, the lack of an ICC allows for a large and evolving blazar population without upsetting the *Fermi* limits on the EGRB and statistics of high-energy blazars.

Based upon the plasma-instability mechanism, we now adopt as a hypothesis that the ultra-relativistic pairs primarily deposit their energy in the IGM via this or a related mechanism. In this paper (Paper II), we explore the impact of this heating on the thermodynamics of the IGM. We estimate the amount of heating provided by the observed TeV blazar population after correcting for the selection effects of the current pencil beam VHEGR observations using the all-sky monitoring of the *Fermi* satellite. We will show that the luminosity density in VHEGRs is of order 0.2% of the quasar luminosity density, which dominates the photoheating rate at low z . We then explore the qualitative and quantitative nature of this heating, which in essence, serves as an alternate feedback mechanism. In particular, TeV blazars deposit heat evenly in a *volumetric* sense, i.e., independent of the local IGM density. Hence, this heating deposits more energy per baryon in low-density regions than in high-density regions, naturally producing an inverted temperature-density relation in voids. With only a minor rescaling of the empirically normalized of observed blazar heating, we find that it is possible to reproduce the inferred inverted temperature-

density relation at $z = 2-3$ (Bolton & Becker 2009; Viel et al. 2009), something which has proven to be a problem within the context of standard reionization models (McQuinn et al. 2009; Bolton & Becker 2009).

In Pfrommer et al. (2012, hereafter Paper III), we will explore the result of this additional IGM heating upon the formation of structure in the Universe. In particular, we will show that the injection of entropy into the IGM by TeV blazars contributes to developing a redshift dependent entropy floor for galaxy clusters and groups at $z \lesssim 2$ and suppresses the formation of dwarfs. We will highlight that the redshift dependent nature of TeV blazar heating in our model suggests a large injection of entropy around $z \sim 1$, which boosts the entropy of late forming objects. This predicted enhanced entropy of young groups is consistent with recent observations that show optically bright and therefore young, groups and clusters are X-ray dim – that is having a lower gas density due to a raised entropy floor. We also will show that TeV blazar heating suppresses the formation of late forming dwarfs both in galactic halos, i.e., the missing satellite problem (Kravtsov 2010), and in voids, i.e., the void phenomenon (Peebles 2001) by raising the temperature of the IGM such that gas cannot collapse to form galaxies.

This work is organized as follows: We first review the fate of energy carried by VHEGR photons in Section 2, discussed in detail in Paper I. We describe how VHEGR photons produce pairs in the IGM and how these ultra-relativistic pair beams are unstable to plasma instabilities. In particular, we highlight the “oblique” instability, which is especially efficient at converting the kinetic energy of the beams into thermal energy in the IGM. Motivated by our review of Paper I, we adopt the assumption that the kinetic energy of the ultra-relativistic pairs is thermalized in the IGM, either via the “oblique” instability or some related mechanism. In Section 3, we estimate the current TeV-blazar IGM heating rate by collating the known extragalactic TeV blazars with a well measured spectrum, accounting for incompleteness (Section 3.1.1). We use the similarity between the luminosity functions of nearby quasars and TeV blazars found in Paper I, to extend the heating rate to $z > 0$ and estimate the TeV-blazar covering fraction (Sections 3.1.2 and 3.2). The implications for the thermal history of low-density regions (less than 10 times the mean density, i.e., $1 + \delta \lesssim 10$) are explored in Section 4. Generally, we find that without any fine tuning it is possible to reproduce the inverted temperature-density relation at $z = 2-3$ inferred by high-redshift Ly α studies (Bolton et al. 2008; Viel et al. 2009), while simultaneously satisfying the temperature constraints at $z = 2$ (e.g., those by Lidz et al. 2010) and leaving the local Ly α forest unaffected.

The results of this work and Paper III assume that the energy of TeV blazars are efficiently thermalized in the IGM. Though we have identified a particularly promising instability, i.e., the “oblique” instability, in Paper I, the particular details by which the energy in ultra-relativistic pairs is thermalized are unimportant. Instead, the results of this work and Paper III depend solely on the gross energetics of the TeV blazars. As a consequence, observations of the thermal history and constraints upon the structures in low-density regions represent an independent empirical probe of the fate of the ultra-relativistic pairs produced by TeV blazars.

For all of the calculations presented below (and in this series) we have assumed the WMAP7 cosmology with $h_0 = 0.704$, $\Omega_{DM} = 0.227$, $\Omega_B = 0.0456$, and $\Omega_\Lambda = 0.728$ (Komatsu et al. 2011).

2. REVIEW OF VHEGR PHOTON PROPAGATION THROUGH THE IGM

The observed extragalactic VHEGR sources are all located at low redshift ($z \lesssim 0.5$). This is due to the annihilation of VHEGRs on the EBL, producing ultra-relativistic e^\pm pairs (see, e.g., Gould & Schröder 1967; Salamon & Stecker 1998; Neronov & Semikoz 2009). Here we describe the fate of these VHEGRs, and the consequences of propagating through the intergalactic medium (IGM) for the pairs they produce. We refer the interested reader to Sections 2 and 3 of Paper I for a more complete discussion of the properties of the generated pairs and the importance and nature of plasma beam instabilities upon their propagation.

VHEGRs are attenuated by the pair production off EBL photons. Namely, when the energies of the VHEGRs (E) and the EBL photon (E_{EBL}) exceed the rest mass energy of the e^\pm pair in the center of mass frame, i.e., $2E E_{EBL}(1 - \cos\theta) > 4m_e^2 c^4$, where θ is the relative angle of propagation in the lab frame, an e^\pm pair can be produced with Lorentz factor $\gamma \simeq E/2m_e c^2$ (Gould & Schröder 1967). An estimate for the mean free path of VHEGR photons is (Paper I)

$$D_{pp}(E, z) = 35 \left(\frac{E}{1 \text{ TeV}} \right)^{-1} \left(\frac{1+z}{2} \right)^{-\zeta} \text{ Mpc}, \quad (3)$$

where the redshift evolution is due to that of the EBL alone, is dependent predominately upon the star formation history, and $\zeta = 4.5$ for $z < 1$ and $\zeta = 0$ for $z \geq 1$ (Kneiske et al. 2004; Neronov & Semikoz 2009)⁴. Relative to the Hubble length, the attenuation length of VHEGRs is very short. In fact, above 100 GeV the Universe is optically thick to sources at $z > 1$ (cf. Franceschini et al. 2008).

Since D_{pp} is much larger than any conceivable source size, and $E_{EBL} \ll E$, locally these pairs necessarily constitute a cold, highly anisotropic beam. The production of pairs by the interaction of VHEGRs with the EBL is opposed by the removal of these pairs by various cooling processes. That is, the evolution of the characteristic pair-beam density at the injection Lorentz factor, n_b , is governed by the Boltzmann equation:

$$\frac{\partial n_b}{\partial t} + \frac{c}{r^2} \frac{\partial r^2 n_b}{\partial r} + \Gamma n_b = \dot{n}_b, \quad (4)$$

where the left-hand side assumes all the pairs are moving away from the VHEGR source relativistically ($v^r = c$ and $p^r = \gamma m_e c$), the right-hand side corresponds to pair production, and Γ is the cooling/removal rate of these pairs. In a homogeneous steady state, the rate of production is balanced by the rate of removal, which gives:

$$n_b \simeq \frac{2F_E}{D_{pp}\Gamma}, \quad (5)$$

where the rate of production is given by $\dot{n}_{beam} = 2(EdN/dE)/D_{pp} = 2F_E/D_{pp}$. Generally, Γ is a function of energy and beam energy and refer the reader to Paper I for additional details. However, for any choice of Γ , the solution to Equation (5) gives $n_b(E, F_E, z)$.

Commonly, it is assumed that the pairs evolve primarily due to an ICC which deposits the energy from the original VHEGR photon near ~ 100 GeV. Note that this is fundamentally radiative; after the VHEGRs are scattered down to 100 GeV they effectively decouple from the Universe. ICCs of these pair beams

⁴ Despite the fact that the EBL contribution from starbursts peaks at $z = 3$ and declines rapidly afterward, galaxies and Type 1 AGNs compensate for the lost flux until $z = 1$. See, for example, Figure 3 from Franceschini et al. (2008).

widely exploited as a possible probe of IGM magnetic fields in the context of the missing inverse Compton features at 100 GeV (see, e.g., Neronov & Vovk 2010; Tavecchio et al. 2010, 2011; Dermer et al. 2011; Taylor et al. 2011; Takahashi et al. 2012; Dolag et al. 2011). The associated cooling rate for this process for pairs with Lorentz factor γ is

$$\Gamma_{\text{IC}} = \frac{4\sigma_T u_{\text{CMB}}}{3m_e c} \gamma \simeq 1.4 \times 10^{-20} (1+z)^4 \gamma \text{ s}^{-1}, \quad (6)$$

where σ_T denotes the Thompson cross section. The strong redshift dependence arises from the rapid increase in the CMB energy density with z ($u_{\text{CMB}} \propto (1+z)^4$).

However, this may not be the dominant process. As we showed in Paper I, plasma beam instabilities are a potential mechanism by which the kinetic energy of the pairs is extracted much more rapidly. The two plasma beam instabilities most frequently discussed, the two stream and Weibel instabilities, are particular limits of a more general instability, differentiated by the direction of the perturbed wave vector with respect to the beam orientation (perpendicular for Weibel, parallel for the two stream; Bret et al. 2005). For dilute beams, by far the most powerful growth occurs at oblique angles, and thus named the “oblique” instability. Paper I and Bret et al. (2010b) gives a more extensive discussion of these three plasma instabilities.

Relative to the laboratory frame, these pair beams are “cold”, i.e., their transverse momentum is much smaller than their parallel momentum, but even the small transverse temperatures that are acquired from pair production for these pair beams are important, placing the oblique instability in the kinetic regime. Here, the oblique instability cooling rate has been numerically measured to be

$$\Gamma_{\text{M,k}} \simeq 0.4 \frac{m_e c^2}{kT_b} \frac{n_b}{n_{\text{IGM}}} \omega_P \simeq 0.4 \gamma \sqrt{\frac{4\pi e^2 n_b^2}{m_e n_{\text{IGM}}}}, \quad (7)$$

where $n_{\text{IGM}} = 2.2 \times 10^{-7} (1+\delta)(1+z)^3 \text{ cm}^{-3}$ is the IGM free-electron number density (assuming full ionization), e is the elementary charge, and we have set the beam temperature in the beam frame to $m_e c^2/k$, characteristic of that induced by pair production, and thus $kT_b = m_e c^2/\gamma$ (Bret et al. 2010a). Both the cold and hot growth rates have been verified explicitly using particle-in-cell (PIC) simulations, though at somewhat less dilute beams than the pair beams from TeV blazars (Bret et al. 2010b).

For the kinetic oblique instability, the cooling rate is

$$\Gamma_{\text{M,k}} \simeq 3.6 \times 10^{-11} (1+\delta)^{-1/4} \left(\frac{1+z}{2} \right)^{(6\zeta-3)/4} \times \left(\frac{EL_E}{10^{45} \text{ erg s}^{-1}} \right)^{1/2} \left(\frac{E}{\text{TeV}} \right)^{3/2} \text{ s}^{-1}, \quad (8)$$

where L_E is the isotropic-equivalent luminosity per unit energy of the VHEGR source. This is a stronger function of photon energy than inverse-Compton cooling, implying that it will eventually dominate at sufficiently high energies, assuming a flat VHEGR spectrum. In addition it is a very weak function of δ , being only marginally faster in lower-density regions, and thus the cooling of the pairs is largely independent of the properties of the background IGM.

The effective cooling rates induced by the “oblique” instability can be obtained by numerically solving Equation (5) for n_b , with $\Gamma = \Gamma_{\text{IC}} + \Gamma_{\text{M,k}}$ as described in Paper I. For the purpose

of this paper, for TeV blazars the effective cooling rate is generally dominated by the “oblique” mode and thus the fraction of VHEGR emission that is effectively thermalized is nearly unity. Therefore, we are justified in assuming that all of the VHEGR emission is thermalized. In Section 3.1.2 we will briefly revisit this assumption at high z , finding again that it is well justified at all z .⁵

However, this may not be the case for all potential VHEGR sources. The physics of the “oblique” instability, like all plasma beam instabilities, depends strongly upon the beam density. For the pair beams that result from VHEGR-EBL photon interactions, the beam density is a function of source luminosity. Hence for sufficiently low luminosity systems, the “oblique” mode grows so slowly that inverse Compton off of the CMB dominates it. This defines a critical isotropic-equivalent luminosity for plasma beam instabilities to be relevant, typically near $10^{42} \text{ erg s}^{-1}$, though depending upon redshift (see Figure 3 of Paper I). For the TeV blazars considered in this paper, this is generally not a concern. However, this will be important in our discussion of alternative VHEGR sources in Section 3.4.

3. TEV BLAZAR HEATING OF THE IGM

As we have argued in Paper I and reviewed in Section 2, plasma instabilities on the pair beam dissipate the bulk of the VHEGR emission. In particular, the “oblique” instability appears to be a promising mechanism by which the ultra-relativistic pair beams that are produced from the interaction of VHEGR and EBL photons blazars are efficiently thermalized and converted to local IGM heating. Henceforth, we will make the assumption for the rest of this work and again in Paper III that the energy of TeV blazars is efficiently thermalized in the IGM. With this stated assumption, we now discuss the sources that dominate the IGM heating rate, estimate the magnitude of the heating rate and its evolution with redshift, and briefly assess the homogeneity with which this new process occurs.

3.1. TeV-Blazar Heating Rates

The local heating rate associated with the dissipation of the high-energy emission from a single blazar is determined by two factors: the rate at which the VHEGRs are converted into pairs and the rate at which the energy of the pairs is subsequently converted locally into heat. The former is determined by the pair-production cross-section. Due to the efficiency of the plasma instabilities in dissipating the beam energy, the latter is set by the ratio of the relevant cooling rates. That is, the single-blazar heating rate is

$$\dot{q} = \int dE \frac{\theta(E)}{D_{\text{pp}}(E, z)} f(F_E, E, z) F_E, \quad (9)$$

where $\theta(E)$ is a dimensionless function due to the pair-creation threshold and which depends upon the shape of the EBL spectrum (we set $\theta(E)$ to vanish for $E < 100 \text{ GeV}$ and be unity otherwise), and

$$f(F_E, E, z) = 1 - f_{\text{IC}} = \frac{\Gamma_{\text{M,k}}}{\Gamma_{\text{IC}} + \Gamma_{\text{M,k}}}, \quad (10)$$

which is a function of F_E , E , and z via the dependence of the cooling rates upon n_b , γ , and z . Generically, f represents the

⁵ We, however, have made the implicit assumption that the nonlinear state of the “oblique” instability removes kinetic energy from the beam at the growth rate of the linear instability.

fraction of pair energy that is thermalized, but we have chosen a specific form of f corresponding to the "oblique" instability to make the discussion below more concrete. While it is also very weakly dependent upon δ , this may be neglected in practice.

Within the linear regime the plasma instabilities responsible for the dissipation of pair beam energy are independent of those arising from beams in substantially different directions. Since the local VHEGR flux is dominated by a number of sources that is small in comparison to that needed to isotropize the beam's phase space, we may treat the resulting evolutions of their associated pair beams independently and sum their resulting heating rates to determine the total heating rate, \dot{Q} .⁶

3.1.1. Estimating the Local Heating Rate

The local heating rate can be estimated in at least two ways, both of which give similar results. First, since the high-energy gamma rays deposit their energy locally, we can identify the local heating rate with the high-energy gamma-ray luminosity density of TeV blazars. In Paper I we showed that this is roughly 2.1×10^{-3} that of quasars, and thus approximately $\sim (0.5\text{--}1.4) \times 10^{38} \text{ erg Mpc}^{-3} \text{ s}^{-1} = (3.4\text{--}9.7) \times 10^{-8} \text{ eV cm}^{-3} \text{ Gyr}^{-1}$, depending upon the minimum luminosity at which the heating mechanism operates.

Alternatively, given a sufficiently complete sample, we can estimate the local heating rate using that implied by the fluxes of the observed TeV blazars. In the present epoch, $f(F_E, E, z) \simeq 1$ at the relevant E , and thus the heating rate takes the particularly simple form:

$$\dot{Q}|_{z=0} \simeq \sum_{\text{AGN}} \int dE \theta \frac{F_{E,i}}{D_{\text{pp}}} . \quad (11)$$

To evaluate this sum, we have collated the presently 46 extragalactic VHEGR sources known.⁷ Of these 46, only 28 have published measurements of their VHEGR flux from a combination of VERITAS, H.E.S.S., and MAGIC observations. For these 28 sources, we have extracted the parametrized spectra assuming the form,

$$\frac{dN}{dE} = f_0 \left(\frac{E}{E_0} \right)^{-\alpha} , \quad (12)$$

where f_0 is the normalization in units of $\text{cm}^{-2} \text{ s}^{-1} \text{ TeV}^{-1}$. The gamma-ray energy flux is trivially related to dN/dE by $F_E = EdN/dE \propto E^{1-\alpha}$, from which we obtain a VHEGR flux,

$$F = E_0 f_0 \int_{100 \text{ GeV}}^{10 \text{ TeV}} dE \left(\frac{E}{E_0} \right)^{1-\alpha} , \quad (13)$$

and for sources with a measured redshift a corresponding isotropic-equivalent luminosity, $L = 4\pi D_L^2 F$, where D_L is the luminosity distance. The resulting f_0 , E_0 , α , F , and L are collected in Table 1. In addition we list the redshift, inferred distance, and absorption-corrected intrinsic spectral index at E_0 ,

⁶ We should note that the if the number of blazars in the sky is so numerous as to make the phase space distribution of beam particles isotropic, certain classes of plasma instabilities – in particular the Weibel instability – will be suppressed. The volume filling factor of a pair beam in phase space is the ratio of perpendicular beam temperature to the beam energy, $kT_b/(m_e c^2) \sim 10^{-6}$ (see Paper I); hence we would need $N \sim 10^{12}$ blazars to isotropize any given point in space. However, as will be shown in Section 3.2 the number of blazars that contribute substantially to the local heating rate is much smaller; hence we believe the local pair distribution function is sufficiently anisotropic.

⁷ See <http://www.mppmu.mpg.de/~rwagner/sources/> for an up-to-date list.

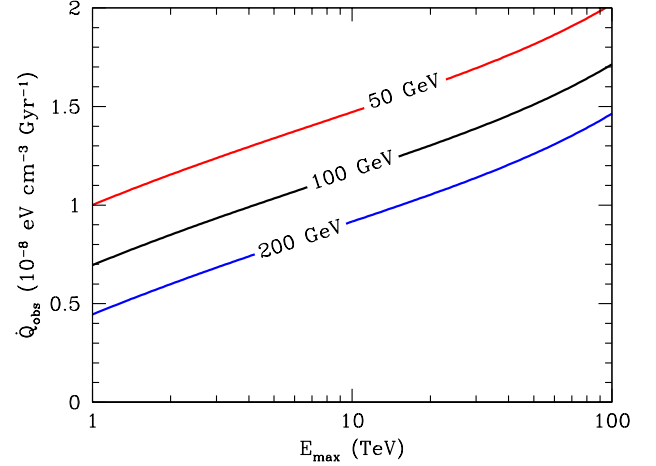


Figure 1. Local heating rate due only the observed TeV blazars as a function of upper-cutoff (E_{max}) and lower-cutoff energies (red, black, and blue lines). In particular, note that the overall value of \dot{Q}_{obs} is relatively insensitive to reasonable variations in the spectral cutoffs.

obtained via

$$\hat{\alpha} = - \left. \frac{d \ln E^{-\alpha} e^{\tau(E,z)}}{d \ln E} \right|_{E_0} \simeq \alpha - \tau(E_0, z) , \quad (14)$$

where $\tau(E, z)$ is the optical depth accrued by a VHEGR emitted at redshift z and with observed energy E .⁸ For high-redshift sources $\hat{\alpha}$ can be less than 2, implying that an intrinsic spectral upper-cutoff must exist. Here we conservatively take this to be at $E \simeq 10 \text{ TeV}$, which is well justified given the distances to the two sources that dominate the observed local TeV flux, Mkn 421 and 1ES 1959+650, though as we shall see below, the heating rate is relatively insensitive to the particular values of the lower and upper spectral cutoffs.

Using the observed VHEGR source in Table 1, the heating rate associated with the 23 IBL/HBL blazars (labeled I and H in the table, see below) is

$$\dot{Q}_{\text{obs}} \simeq \sum_{\text{obs AGN}} \frac{E_0^2 f_0}{D_{\text{pp}}(E_0, 0)} \int_{100 \text{ GeV}}^{10 \text{ TeV}} \frac{dE}{E_0} \left(\frac{E}{E_0} \right)^{2-\alpha} . \quad (15)$$

Note that for $\alpha \simeq 3$, characteristic of the two dominant TeV sources, this depends logarithmically upon the lower and upper spectral cutoffs. The resulting \dot{Q}_{obs} is shown in Figure 1 as a function of the upper spectral cutoff, E_{max} for a handful of different lower cutoffs, ranging from 50 GeV to 200 GeV. For our fiducial values, $\dot{Q}_{\text{obs}} = 1.2 \times 10^{-8} \text{ eV cm}^{-3} \text{ Gyr}^{-1}$, with this only weakly depending upon the various cutoffs, changing by at most by a factor of 2 over the reasonable ranges. Hence, for the remainder of this work, we choose a lower spectral cutoff of 100 GeV.

To complete this estimate, we now correct for the selection effects of VHEGR observations. To correct for the pointed nature of VHEGR observations, we rely on the all-sky GeV gamma-ray observations from the Fermi satellite (Abdo et al. 2010a) of TeV blazar. Those belong to 2 subclasses of blazars, namely high-energy peaked BL Lacs (HBL) and the somewhat less efficient accelerators, intermediate-energy peaked BL Lacs

⁸ This differs subtly from the definition of $\tau_E(E, z)$ in Paper I, where there we set E to the emitted energy of the gamma ray. A full definition at arbitrary observer redshift can be found in Equation (A2).

Table 1
List of TeV Sources with Measured Spectral Properties in Decreasing 100 GeV–10 TeV Flux Order

Name	z	D_C^a	f_0^b	E_0^c	α^d	F^e	$\log_{10} L^f$	$\hat{\alpha}^g$	\dot{q}^h	Class ⁱ	Reference
Mkn 421	0.030	129	68	1	3.32	1.7×10^3	45.6	3.15	44	H	Chandra et al. (2010)
1ES 1959+650	0.047	201	78	1	3.18	1.6×10^3	45.9	2.90	47	H	Aharonian et al. (2003)
1ES 2344+514	0.044	190	120	0.5	2.95	2.3×10^2	45.0	2.82	9.2	H	Albert et al. (2007c)
Mkn 501	0.034	150	8.7	1	2.58	85	44.4	2.39	6.0	H	Huang et al. (2009)
3C 279	0.536	2000	520	0.2	4.11	68	46.9	2.53	1.0	Q	MAGIC Collaboration et al. (2008)
PKS 2155-304	0.116	490	1.81	1	3.53	64	45.4	2.75	1.4	H	HESS Collaboration et al. (2010)
PG 1553+113	> 0.09	> 380	46.8	0.3	4.46	41	> 44.9	< 4.29	< 3.88	H	Aharonian et al. (2008b)
W Comae	0.102	430	20	0.4	3.68	31	44.9	3.41	0.6	I	Acciari et al. (2009b)
3C 66A	0.444	1700	40	0.3	4.1	28	46.3	2.43	0.4	I	Acciari et al. (2009c)
1ES 1011+496	0.212	870	200	0.2	4	26	45.5	3.66	0.4	H	Albert et al. (2007b)
1ES 1218+304	0.182	750	11.5	0.5	3.07	24	45.4	2.37	0.8	H	Acciari et al. (2010a)
Mkn 180	0.045	190	45	0.3	3.25	20	44.0	3.17	0.6	H	Albert et al. (2006)
1H 1426+428	0.129	540	2	1	2.6	20	45.0	1.71	1.4	H	Aharonian et al. (2002)
RGB J0710+591	0.125	520	1.36	1	2.69	15	44.8	1.83	0.9	H	Acciari et al. (2010c)
1ES 0806+524	0.138	580	6.8	0.4	3.6	10	44.7	3.21	0.2	H	Acciari et al. (2009a)
RGB J0152+017	0.080	340	0.57	1	2.95	8.5	44.1	2.45	0.3	H	Aharonian et al. (2008a)
1ES 1101-232	0.186	770	0.56	1	2.94	8.2	44.9	1.50	0.3	H	Aharonian et al. (2007a)
1ES 0347-121	0.185	770	0.45	1	3.1	8.2	44.9	1.67	0.3	H	Aharonian et al. (2007b)
IC 310	0.019	83	1.1	1	2.0	8.1	42.8	1.90	0.1	H	Aleksić et al. (2010)
PKS 2005-489	0.071	300	0.1	1	4.0	8.0	44.0	3.56	0.1	H	Aharonian et al. (2005)
MAGIC J0223+430	—	—	17.4	0.3	3.1	7.6	—	< 3.1	0.2	R	Aliu et al. (2009)
1ES 0229+200	0.140	590	0.7	1	2.5	6.4	44.5	1.51	0.5	H	Aharonian et al. (2007c)
PKS 1424+240	< 0.66	< 2400	51	0.2	3.8	6.3	< 46.1	> 1.42	0.1	I	Acciari et al. (2010b)
M87	0.0044	19	0.74	1	2.31	5.9	41.4	2.29	0.6	R	Acciari et al. (2008)
BL Lacertae	0.069	290	0.3	1	3.09	5.4	43.8	2.67	0.2	L	Albert et al. (2007a)
H 2356-309	0.165	690	0.3	1	3.09	5.4	44.6	1.86	0.2	H	Aharonian et al. (2006b)
PKS 0548-322	0.069	290	0.3	1	2.86	4.0	43.7	2.44	0.2	H	Aharonian et al. (2010)
Centaurus A	0.0028	12	0.245	1	2.73	2.8	40.7	2.72	0.2	R	Raue et al. (2010)

^a Comoving distance in units of Mpc

^b Normalization of the observed photon spectrum that we assume to be of the form $dN/dE = f_0(E/E_0)^{-\alpha}$, in units of $10^{-12} \text{ cm}^{-2} \text{ s}^{-1} \text{ TeV}^{-1}$

^c Energy at which we normalize the spectrum, in units of TeV

^d Observed spectral index at E_0

^e Integrated energy flux between 100 GeV and 10 TeV, in units of $10^{-12} \text{ erg cm}^{-2} \text{ s}^{-1}$

^f Inferred isotropic integrated luminosity between 100 GeV and 10 TeV, in units of erg s^{-1}

^g Inferred intrinsic spectral index at E_0

^h Local plasma-instability heating rate in units of $10^{-10} \text{ eV cm}^{-3} \text{ Gyr}^{-1}$

ⁱ H, I, L, Q, and R correspond to high-energy, intermediate-energy, low-energy peaked BL Lacs, flat spectrum radio quasars, and radio galaxies of Faranoff-Riley Type I (FR I), respectively.

(IBL) which are, in some cases, also able to reach energies beyond 100 GeV. Outside of the Galactic plane, *Fermi* observes 118 high-synchrotron peaked (HSP) blazars and a total of 46 high-synchrotron peaked (ISP) blazars.⁹ Roughly half of the latter are likely to emit VHEGRs as indicated by their flat spectral index between 0.1 and 100 GeV, $\Gamma \lesssim 2$ (see the spectral index distribution of Figure 14 in Abdo et al. (2009a)). Of these potential 141 TeV blazars, only 22 have also been coincidentally identified as TeV blazars (out of a total of 28 coincident TeV sources), while there are a total of 33 known TeV blazars (29 HBL, 4 IBL). If these 141 sources are all TeV emitters, but have not been detected due to incomplete sky coverage of current TeV instruments, then the selection factor is $\eta_{\text{sel}} = 141/33 = 4.3$. In addition, the duty cycle of coincident GeV and TeV emission is $\eta_{\text{duty}} = 33/22 = 1.5$. Here we assume that the luminosity distribution of observed VHEGR sources reflects the true distribution after correcting for the effects of flux limitations in the observations. That this may be done is justified empirically in Section 5.1.2 of Paper I, and demonstrated explicitly in Figure 5 of Paper I. Thus, we may use constant correction factors (independent of luminosity) to estimate the true distribution. Finally, by excluding the Galactic plane for galactic latitudes $b < 10^\circ$, this is an underestimate by roughly $\eta_{\text{sky}} = 1.17$. Taken together, the true heating rate in our

“standard” model is then:

$$\dot{Q}|_{z=0} \simeq 7 \times 10^{-8} \left(\frac{\eta_{\text{sys}}}{0.8} \right) \times \left(\frac{\eta_{\text{sel}}}{4.3} \right) \left(\frac{\eta_{\text{duty}}}{1.5} \right) \left(\frac{\eta_{\text{sky}}}{1.2} \right) \text{ eV cm}^{-3} \text{ Gyr}^{-1}, \quad (16)$$

where η_{sys} is a remaining coefficient of order unity correcting for systematic uncertainties. These include corrections to the spectral model we currently use and the corrections to the completeness of the *Fermi* sample of HBLs and IBLs in accounting for the complete population of VHEGR sources. The fact that there are already 4 radio galaxies of Faranoff-Riley Type I (FR I), 2 flat spectrum radio quasars, and 2 starburst galaxies emitting VHEGRs implies that we are probably too conservative in accounting for all the VHEGR sources. To explore the effects of the variation in the heating rate, we also adopt an “optimistic” heating model that is normalized to fit the observed IGM inverted temperature-density relation (Viel et al. 2009). This “optimistic” model has $\eta_{\text{sys}} = 1.6$ yielding a heating rate of $\dot{Q}|_{z=0} = 1.4 \times 10^{-7} \text{ eV cm}^{-3} \text{ Gyr}^{-1}$.

In estimating \dot{Q} from Equation (11) we have made a number of implicit assumptions. First, we have assumed that the observed distribution of TeV blazars locally is representative of the average distribution at *any given point* in the Universe. Since the blazars that have been observed locally go out to $z \approx 0.5$, we believe this is a relatively safe assumption. Sec-

⁹ The source classes of HSP/ISP are very similar to the commonly used HBL/IBL classes. Hence we identify both for the remainder of this work.

ond, we have assumed that the current sample of blazars is sufficiently flux-complete to dominate the heating rate at Earth. That is, we have assumed that the effective flux limit of the current generation of Cerenkov telescopes is low enough that it captures the bulk of the sources responsible for the local heating of the IGM. That this is the case is less clear, and will be the subject of Section 3.2 and the Appendix in some detail. Unfortunately, since the constant of proportionality relating the local TeV blazar and quasar luminosity densities is obtained using the observed set of blazars, our two estimates are strongly correlated.

Nevertheless, this provides a convenient lower limit upon \dot{Q} , and we use this heating rate, which we denote the "standard" heating rate, as the mean heating rate of any fluid element in the present-day Universe. Over a Hubble time, the total heat deposited per unit volume is then roughly

$$u_{\text{tot}}|_{z=0} \simeq \frac{\dot{Q}|_{z=0}}{H_0} \approx 10^{-6} \text{ eV cm}^{-3}, \quad (17)$$

which is sufficient to raise the temperature of $1 + \delta = 0.1$ regions to approximately $1.7 \times 10^5 \text{ K}$, and thus dramatically alter the thermal history of voids.

3.1.2. Estimating the $z > 0$ Heating Rate

Extrapolating the above estimate to $z > 0$ requires understanding how the TeV blazar properties and population have evolved, as well as the evolution in $f(F_E, E, z)$. Generally, the average heating rate is given by

$$\dot{Q} = \int dV d\log_{10} L d\alpha d\Omega \tilde{\phi}_B(z; L, \alpha, \Omega) \frac{\Omega}{2\pi} \dot{q}, \quad (18)$$

where $\tilde{\phi}_B(z; L, \alpha, \Omega, z)$ is the physical number density of blazars at a given redshift per unit logarithmic isotropic-equivalent luminosity, spectral index, and blazar jet opening angle (we've assumed all jets are symmetric). We make the simplifying assumption that $\tilde{\phi}_B$ is separable into components describing the evolving luminosity density distribution, $\tilde{\phi}_B(z, L)$, and a static, unit-normalized spectral distribution, $\varphi_B(\alpha, \Omega)$, where $\tilde{\phi}_B(z; L, \alpha, \Omega) = \tilde{\phi}_B(z, L) \varphi_B(\alpha, \Omega)$. This produces,

$$\dot{Q} = \int d\log_{10} L L \tilde{\phi}_B(z, L) \times \int D^2 dD d\alpha d\Omega \int dE \frac{\theta}{D_{\text{pp}}} f \frac{L_E e^{-D/D_{\text{pp}}}}{L D^2}, \quad (19)$$

where the bulk of the redshift and luminosity dependence is now contained in the outer-most integral over $\log_{10} L$, and we have used $\tau_E \simeq D/D_{\text{pp}}$ (since the heating is dominated by nearby objects, for simplicity we do not distinguish between different cosmological distance definitions, though see the Appendix for a more careful treatment). If there were no redshift or flux dependence in the remaining terms, it would be possible to simply normalize the heating rate by $\dot{Q}|_{z=0}$ and the estimated TeV-blazar luminosity density, which we define to be

$$\tilde{\Lambda}_B(z) \equiv \int_{\log_{10} L_{\text{min}}}^{\infty} d\log_{10} L L \tilde{\phi}_B(z, L), \quad (20)$$

where $L_{\text{min}} \simeq 3 \times 10^{42} \text{ erg s}^{-1}$ is chosen so that the plasma instabilities operate efficiently at all redshifts of interest. However,

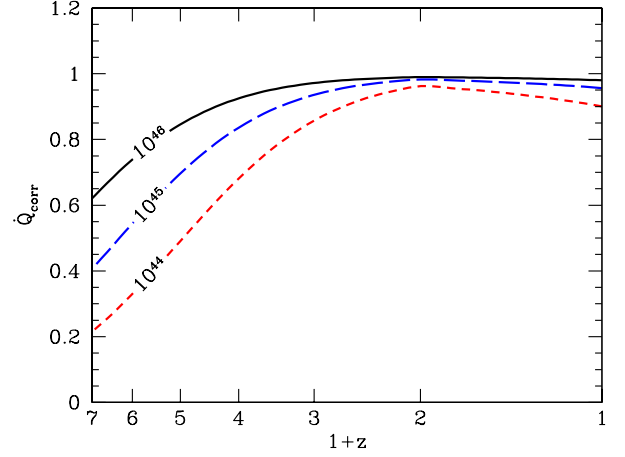


Figure 2. Heating correction due to the intrinsic evolution of the plasma instability and inverse-Compton cooling rates as a function of redshift. Shown are the corrections for $L = 10^{46} \text{ erg s}^{-1}$ (black solid), $10^{45} \text{ erg s}^{-1}$ (blue long-dashed), and $10^{44} \text{ erg s}^{-1}$ (red short-dashed). For comparison, the TeV blazars that dominate the heating locally have luminosities of roughly $5 \times 10^{45} \text{ erg s}^{-1}$.

this is not entirely the case since $f(F_E, E, z)$ retains some dependence upon z , and thus we set

$$\dot{Q} = \frac{\tilde{\Lambda}_B(z)}{\tilde{\Lambda}_B(0)} \dot{Q}|_{z=0} \dot{Q}_{\text{corr}}(z), \quad (21)$$

where \dot{Q}_{corr} provides a correction due to the changing strength of the pair beam dissipation mechanism in comparison to inverse-Compton cooling.

The VHEGR flux at Earth is dominated by a handful of very bright sources for which the absorption corrected $\alpha \simeq 3$ at 1 TeV and isotropic-equivalent luminosity $5 \times 10^{45} \text{ erg s}^{-1}$. This simplifies the estimation of \dot{Q}_{corr} significantly, giving

$$\dot{Q}_{\text{corr}}(z) \simeq \frac{\iint dE dD \frac{\theta E^{-2}}{D_{\text{pp}}} e^{-D/D_{\text{pp}}} f\left(\frac{L_E e^{-D/D_{\text{pp}}}}{4\pi D^2}, E, z\right)}{\int dE \theta E^{-2}}, \quad (22)$$

in which the form and magnitude of L_E is fixed. The resulting correction factors are shown in Figure 2 for isotropic-equivalent luminosities above 100 GeV ranging from $10^{44} \text{ erg s}^{-1}$ to $10^{46} \text{ erg s}^{-1}$. Generally, \dot{Q}_{corr} makes a small ($\lesssim 15\%$) correction following the peak of the quasar luminosity function ($z = 2$), though can grow to as much as 80% by $z = 6$ for dim objects. However, since we will be primarily interested in bright blazars at $z \lesssim 4$, \dot{Q}_{corr} modifies the heating rate at relevant redshifts by $\lesssim 50\%$ (see also Section 3.3). Thus, given the comparatively larger uncertainties associated with the TeV blazar luminosity function, plasma heating mechanism, and additional potential VHEGR sources, we neglect \dot{Q}_{corr} in what follows.

Therefore, obtaining the heating rate as a function of z is reduced to estimating $\tilde{\Lambda}_B(z)/\tilde{\Lambda}_B(0)$, the normalized evolution of the blazar luminosity density. However, no VHEGR emitting blazars are known beyond $z \simeq 0.7$, presumably due to the pair-creation absorption associated with propagation through the EBL. As a consequence, nothing is known about $\tilde{\Lambda}_B(z)$ at high redshifts directly. Nevertheless, in Paper I we showed that

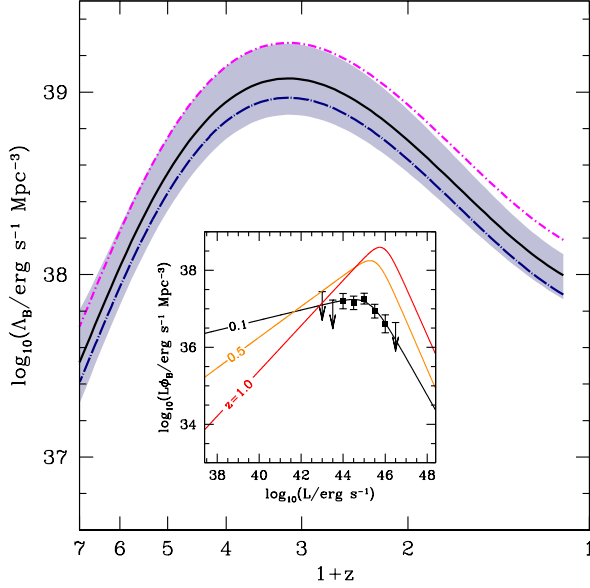


Figure 3. Blazar luminosity density (in comoving units, with $\eta_{\text{sys}} = 1$) as a function of redshift. The shaded region represents the $1\text{-}\sigma$ uncertainty that results from a combination of the uncertainty in the number of bright blazars that contribute to the local heating and in the uncertainties in the Hopkins et al. (2007) quasar luminosity density to which we normalize. Our optimistic and standard models, defined in Section 3.1.1, are shown by the magenta short-dash-dot and blue long-dash-dot lines. Insert: Comparison between the observed blazar luminosity function (data points with one sigma error bars and upper limits) with the quasar luminosity function that has been shifted by a factor of 2.1×10^{-3} in luminosity density and 0.55 in luminosity. This insert is a simplified reproduction of Figure 5 of Paper I.

a close relationship between $\tilde{\phi}_B$ and the quasar luminosity function of Hopkins et al. (2007), $\tilde{\phi}_Q$, exists at low z :

$$\tilde{\phi}_B(0.1, L) \simeq 3.8 \times 10^{-3} \tilde{\phi}_Q(0.1, 1.8L). \quad (23)$$

The insert in Figure 3 shows a comparison between the observed TeV-blazar luminosity function, calculated from the distribution of the sources in Table 1 and applying an empirically determined flux limit of $4.19 \times 10^{-12} \text{ erg cm}^{-2} \text{ s}^{-1}$, with $\phi_B(0.1, L)$ (for a full description of how the luminosity function was formed, and how it compares to ϕ_Q , see Section 5 of Paper I). Furthermore, we showed that once the ICCs are suppressed by the plasma beam instabilities (or some analogous mechanism), extending this relationship to high- z was in excellent agreement with the best current constraints upon the high- z TeV blazar population: the *Fermi* TeV blazar statistics and the *Fermi* measurement of the extragalactic gamma-ray background (between 100 MeV and 100 GeV). Thus, we estimate $\Lambda_B(z) \simeq 2.1 \times 10^{-3} \Lambda_Q(z)$, shown in Figure 3, where $\Lambda_Q(z)$ is the luminosity density of quasars.

Figure 3 shows that employing the quasar luminosity density to estimate the heating rates has profound consequences. In particular, the inferred luminosity density of TeV blazars (solid line) rises rapidly with increasing z , with the comoving density increasing by roughly a factor of ~ 10 by $z = 2$ (see also Figure 8 of Hopkins et al. 2007). In physical units this corresponds to a increase by a factor of nearly 300. Thus, we expect an increase in the local heating rate by a similar factor over the presently estimated value near $z = 2$.

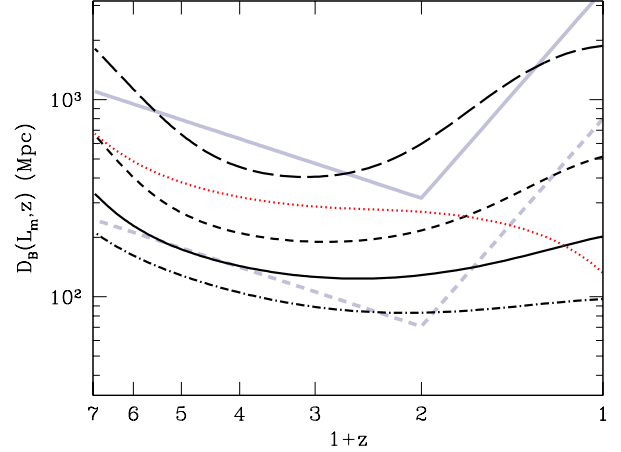


Figure 4. Comoving mean separation of blazars with isotropic-equivalent luminosities (L , in the 100 GeV–10 TeV band) above $L_m = 10^{43} \text{ erg s}^{-1}$ (dot-dash), $10^{44} \text{ erg s}^{-1}$ (solid), $10^{45} \text{ erg s}^{-1}$ (short-dash), $10^{46} \text{ erg s}^{-1}$ (long-dash), and the local luminosity-weighted median luminosity of TeV blazars (red dot), as functions of redshift. For reference the spectrally averaged (with $\alpha = 3$) mean free path, D_{pp} , and the local mean free path for a 1 TeV gamma ray are shown by the grey solid and dashed lines, respectively. For sources with a spectral break between 100 GeV and 1 TeV, we anticipate the effective mean free path to lie between these.

3.2. Homogeneity of TeV-Blazar Heating

We now investigate the assumption of even heating as a prelude to our simple one-zone model of the IGM. In lieu of large-scale simulations, the homogeneity of the heating due to TeV blazars is difficult to assess for a variety of reasons. First, the duty cycle of the TeV blazars is unknown. Second, the density at high redshifts is poorly constrained. Third, the importance of clustering bias is unclear. Fourth, it is difficult even to define which blazars are relevant, e.g., which luminosity range contributes the bulk of the local heating. Nevertheless, we make an attempt to roughly characterize the possible range in the stochasticity of the local heating rates via a number of different estimates.

3.2.1. Mean Separation of TeV Blazars

We begin by estimating the instantaneous comoving mean separation of *visible* blazars above various luminosity thresholds,

$$D_B(L_m, z) = (1+z) \left[\int_{\log_{10} L_m}^{\log_{10} L_M} \tilde{\phi}_B(L, z) d\log_{10} L \right]^{-1/3}, \quad (24)$$

where the precise value of L_M is unimportant as long as it is above the peak of the luminosity function; here we choose $L_M = 2 \times 10^{46} \text{ erg s}^{-1}$, consistent with the theoretically expected upper limit of TeV blazar luminosities. Since we have determined $\tilde{\phi}_B$ from the observed blazar population, and are making use of the isotropic-equivalent luminosities, this is independent of the blazar jet opening angle; smaller opening angles will result in a correspondingly larger number of objects such that the total number seen is unchanged, and therefore D_B is fixed. A comparison between D_B and the mean free path of VHEGRs is shown in Figure 4. Because D_{pp} varies dramatically from 100 GeV to 10 TeV, for this purpose, we define a spectrally av-

eraged mean free path, \bar{D}_{pp} , determined implicitly by

$$\int_{100 \text{ GeV}}^{10 \text{ TeV}} dE E^{1-\alpha} e^{-\bar{D}_{pp}(z)/D_{pp}(E,z)} = e^{-1} \int_{100 \text{ GeV}}^{10 \text{ TeV}} dE E^{1-\alpha}, \quad (25)$$

in which we choose $\alpha = 3$ based upon the local TeV blazar sample. This is roughly the e -folding distance of the entire spectral band, shown in Figure 4 by the grey solid line, and in practice is quite close to $D_{pp}(225 \text{ GeV}, z)$. If the intrinsic TeV blazar spectra peak above 100 GeV, our estimate of the typical VHEGR mean free path could be significantly too large; thus we also compare D_B to D_{pp} at 1 TeV (the grey dashed line in Figure 4), providing an extreme lower-bound upon the spectrally averaged mean free path in practice. The rapid increase of the density of EBL photons with z , associated with the larger star formation rate in the recent past, results in a substantially reduced D_{pp} by $z = 1$. Prior to $z = 1$, the physical number density of EBL photons remains nearly constant, and thus $D_{pp} \propto (1+z)$ in comoving units.

In the present epoch, \bar{D}_{pp} is quite large, and thus despite their sparsity the mean separation of even bright blazars ($10^{46} \text{ erg s}^{-1}$) is less than \bar{D}_{pp} . This remains true for objects with luminosities $\leq 10^{45} \text{ erg s}^{-1}$, which includes the local luminosity-weighted median TeV blazar luminosity, $L_{0.5}(z)$, defined such that

$$\int_{\log_{10} L_{0.5}(z)}^{\log_{10} L_M} L \tilde{\phi}_B(L, z) d\log_{10} L = 0.5 \tilde{\Lambda}_B(z). \quad (26)$$

Hence, locally, we expect blazar heating to be quite uniform.

At high redshift matters change somewhat. Until $z = 1$, $\bar{D}_{pp}(z)$ and $D_{pp}(1 \text{ TeV}, z)$ both decrease more rapidly than D_B . For $z > 1$, in comoving units $\bar{D}_{pp}(z)$ and $D_{pp}(1 \text{ TeV}, z)$ increase slowly, though at a marginally larger rate than D_B . As a result, near $z \sim 1$ the mean separation of TeV blazars is largest in comparison to the VHEGR mean free path. Thus, the mean separation between objects more luminous than $10^{46} \text{ erg s}^{-1}$ is larger than \bar{D}_{pp} near $z \sim 1$. Nonetheless, when the lower luminosity limit is dropped to $10^{45} \text{ erg s}^{-1}$ or below, generally $D_B(z) < \bar{D}_{pp}(z)$ for all $z < 6$. Similarly, the mean separation between blazars more luminous than $L_{0.5}(z)$ is also smaller than our estimate of \bar{D}_{pp} for the relevant redshift range. Hence we may expect that nearly all patches of the Universe will be illuminated by at least one luminous TeV blazar following $z \sim 6$.

3.2.2. Estimates of the Number of TeV Blazars that Contribute Significantly to the Heating Rate

Closely related to the mean separation is the number of blazars within the $\bar{\tau} \simeq D/\bar{D}_{pp} = 1$ surface (defined explicitly in the Appendix) above some luminosity limit. Figure 5 shows these for objects with luminosities above $10^{45} \text{ erg s}^{-1}$ (blue short-dash), and $L_{0.5}$ (red dot). While these may be roughly inferred from the associated mean separations in Figure 4, they differ slightly from $(4\pi/3)(\bar{D}_{pp}/D_B)^3$ due to the rapidly evolving \bar{D}_{pp} and blazar population combined with the finite look-back time in the integral. At $z = 0$ both are well above unity, with the luminosity-weighted median value substantially exceeding our estimate of roughly 170 visible extragalactic TeV blazars.¹⁰ However, since generally $\bar{D}_{pp}(z) \simeq 4.4 D_{pp}(1 \text{ TeV}, z)$

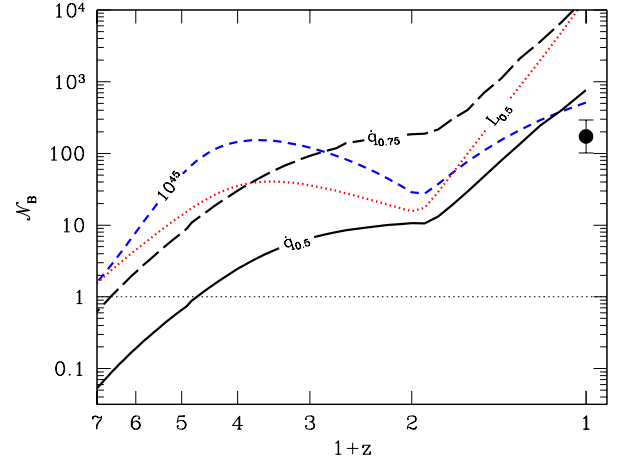


Figure 5. Number of TeV blazars, estimated in various ways, that contribute to the heating of a given patch as a function of redshift. Definitions for \mathcal{N}_B include: the number of blazars with intrinsic isotropic-equivalent luminosities above $10^{45} \text{ erg s}^{-1}$ within the $\bar{\tau} = 1$ surface (blue short-dash), the number of blazars with luminosities above that luminosity-weighted median value at each redshift within the $\bar{\tau} = 1$ surface (red dot), and the number of blazars with individual heating rates that exceed that above which 50% and 75% of the total heating is produced (black solid and long-dash, respectively). For comparison, our estimate of the completeness-corrected number of TeV blazars that are presently observable in the TeV is shown by the filled back point, with error bars denoting the Poisson uncertainty only.

not all of the blazars that contribute to the local heating are expected to appear as strong TeV sources.

The low- z behavior of the number of blazars is dictated by the rapid evolution in D_{pp} , associated with the recent rapid variation in the star formation rate (and thus the number density of EBL photons). Prior to $z = 1$, the EBL density, and hence D_{pp} , is roughly constant in physical units, and the evolution number of visible blazars becomes indicative of the underlying evolution of blazar population. At all $z < 6$ these estimates of the number of blazars responsible for the bulk of the heating, \mathcal{N}_B , exceed unity, implying only a small fractional spatial variation in the blazar heating rate. However, while the luminosity-weighted median estimate of \mathcal{N}_B does give some idea of which population is responsible for most of the TeV blazar luminosity density, neither encapsulates the population responsible for the majority of the local heating. Thus, if the local heating were dominated by a handful of luminous sources, it is possible for the stochasticity to be much larger.

Therefore, we show a third estimate of \mathcal{N}_B , corresponding to the number of sources with q_s larger than the heating-rate-weighted median value (see the Appendix for a precise definition). That is, at a given redshift, the \mathcal{N}_B sources with the highest q_s generate half of the total heating rate. Thus, if a single source were to dominate the local heating rate, \mathcal{N}_B would be considerably less than unity, indicating a large degree of variability. However, below $z \sim 3.5$ this is not the case; the fractional heating rate-defined \mathcal{N}_B is considerably larger than unity. At high redshifts the heating rate becomes increasingly dominated by more distant, luminous, and rarer objects, departing from the previous estimate of \mathcal{N}_B .

Nevertheless, while for $z \gtrsim 3.5$ few sources contribute nearly half of the heating rate, the total heating rate must be comparable to the total VHEGR luminosity density of the blazars. Therefore, the total number of contributing objects must be similar to the number of visible blazars above the luminosity-weighted median L (i.e., the red dotted line in Figure 5). As a

¹⁰ Recall that in Table 1 we have listed 23 TeV Blazars, but a correction factor of 7.5 needs to be applied to account for the incompleteness of present TeV surveys.

consequence, the number of relevant sources must rapidly rise with decreasing fractional heating rate. This is explicitly indicated by the dashed line in Figure 5, which shows the number of sources responsible for 75% of the local heating rate.

In any case, it is clear that for the redshifts at which blazar heating is likely to be important, $z \lesssim 4$, the heating rate will be relatively uniform. Between $z \sim 4$ it may experience order 50% fluctuations, and by $z \sim 6$ will exhibit order unity deviation. However, we note that all of our estimates of the heating inhomogeneity are predicated upon the assumption that the $\tilde{\phi}_B$ accurately represents the distribution of blazars, and has the associated considerable uncertainties. For a more thorough discussion of different estimates of the number of contributing blazars, and a discussion of which blazars dominate the heating rate at a given redshift, see the Appendix.

In addition to the statistics of blazars, the homogeneity also depends upon the intrinsic variability of TeV blazars. During the time that the TeV blazars have been observed their VHEGR emission has remained remarkably stable. However, this provides only a weak lower limit (~ 4 yr) upon the variability timescale in these objects (Dermer et al. 2011). In addition to depending upon the properties of the source itself, the variability of TeV blazars depends upon the primary emission mechanism responsible for the VHEGR component of TeV blazars. There are two classes of inverse-Compton models to explain the VHEGR emission:

1. *Synchrotron self-Compton (SSC) model:* In this model, the synchrotron radiation field is Compton up-scattered to TeV energies by a relativistic electron population (Jones et al. 1974; Ghisellini & Maraschi 1989). Recent work has led to the conclusion that a simple homogeneous, one-zone, SSC model cannot explain the SED of the majority of blazars (see Figure 36 of Abdo et al. 2010b). However, models with multiple SSC components are consistent with the blazar SEDs. Typically these invoke a steady, primary SSC component which peaks at the IR/optical (S) and γ -ray band (IC), and a second more energetic and usually more variable component, which peaks in the UV or X-ray band (S) and at GeV/TeV energies (IC). The variability of this energetic component increases the probability that a given patch of the IGM will see a TeV blazar during its history, resulting in larger homogeneity in the blazar heating.
2. *External radiation Compton (ERC) scenario:* this model proposes that the relativistic jet electrons Compton scatter an external radiation field (Sikora et al. 1994; Dermer & Schlickeiser 2002) from the accretion disk or the dusty torus surrounding it. In the first case, the disk generates UV seed photons which are then reflected toward the jet by the broad line region within a typical distance from the accretion disk of the order of 1 pc. In the second case, the dusty torus could provide IR seed photons that are emitted at larger distances from the jet. In any of these ERC models, the VHEGR emission is expected to be very steady, implying long-lived TeV blazars, resulting in more patchy blazar heating.

We leave detailed studies of the inhomogeneity in the blazar heating rate resulting from intrinsic inhomogeneity and variability in the spatial distributions of the blazars themselves for future work.

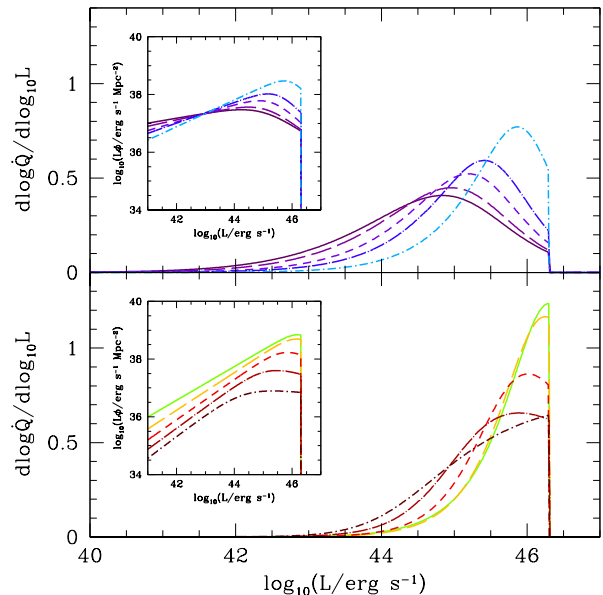


Figure 6. $d \log \dot{Q} / d \log_{10} L$ as defined in Section A.3.2 for the TeV blazars responsible for half of the total heating rate for a number of redshifts (top: from violet blue to light-blue: $z_0 = 0$ (solid), 0.1 (long-dash), 0.3 (short-dash), 0.5 (long-dash-dot), and 1.0 (short-dash-dot); bottom: from green to dark-red: $z_0 = 2$ (solid), 3 (long-dash), 4 (short-dash), 5 (long-dash-dot), and 6 (short-dash-dot)). For reference, $L\phi_B(z_0, L)$ is shown in the inset (in comoving units).

3.3. Properties of the Blazars Responsible for the Heating

In our discussion of the homogeneity of blazar heating we have necessarily attempted to define a class of objects responsible for the bulk of the heating. This is most directly done by considering those TeV sources which produce, say, 50% of the total heating rate at a given observer redshift. Given this population, we may also now address the properties of the most relevant sources themselves; i.e., we can identify which types of TeV blazars dominate the heating. As we have already mentioned, this cannot be too different from the set of blazars which dominate the luminosity density. We address this question in some detail in the Appendix, including constructing a simple analytical toy model.

Figure 6 shows the luminosity distribution of the heating-rate integrand once integrated over distance and assuming our form for $\tilde{\phi}_B(z, L)$ (see the Appendix for a precise definition). The upper-half of the heating rate is dominated by sources with luminosities of approximately $10^{45} \text{ erg s}^{-1}$ at low redshifts, and rises to $10^{46} \text{ erg s}^{-1}$ by $z \sim 2$ before declining slightly thereafter. This evolution is driven both by the changing shape and the changing normalization of $\tilde{\phi}_B$ with redshift. At all redshifts this is larger than the median luminosity. Thus, generally it appears that the heating is due predominantly to high-luminosity objects. Due to the relatively small \bar{D}_{pp} , these are also necessarily nearby.

3.4. Other Potential VHEGR Sources

Up to now, our focus on the TeV-blazars is motivated by the fact that the vast majority of extragalactic VHEGR sources observed are blazars. Other potential source of VHEGR emission exist and so we will discuss these sources in this section. In assessing their potential contribution in VHEGRs, however, we find that these VHEGR sources are subdominant.

3.4.1. Starburst Galaxies

Starburst galaxies are characterized by the presence of rapid star formation, and hence, are sites of numerous supernovae. Supernovae are known to be efficient particle accelerators, and are presumed to be the primary source of the galactic cosmic rays. As cosmic rays can produce VHEGRs, starburst galaxies are potentially bright VHEGR sources.

While many starburst galaxies contain active AGN, that may also emit VHEGRs, unambiguous VHEGR emission from the starburst itself has been seen in at least two cases, M82 and NGC 253, with $E > 100$ GeV luminosities of $5 \times 10^{39} \text{ erg s}^{-1}$ and $2 \times 10^{39} \text{ erg s}^{-1}$, respectively (VERITAS Collaboration et al. 2009; Acero et al. 2009). The luminosity of these two sources are dwarfed by the local TeV blazars, and thus the VHEGR flux from M82 and NGC 253 does not contribute to the heating of the local IGM. In addition, their VHEGR luminosity produces a pair beam which is too dilute for plasma processes such as the "oblique" instability to beat cooling via inverse Compton. Hence, they do not contribute to the local VHEGR flux.

However, very high star-forming systems such as the ultra-luminous infrared galaxies (ULIRGs) where $L_{\text{IR}} > 10^{12} L_{\odot}$ and L_{IR} is the bolometric infrared luminosity ($5 \mu\text{m} < \lambda < 1000 \mu\text{m}$), may evade this constraint. If the VHEGR emission from starburst galaxies is due to cosmic rays accelerated by supernovae, the VHEGR luminosity above 100 GeV, L is then proportional to the star formation rate. For starbursts, this is linearly related to the continuum infrared luminosity (Kennicutt 1998). Thus, normalizing by M82 and NGC 253, we have

$$L \simeq 6 \times 10^{40} \left(\frac{L_{\text{IR}}}{10^{12} L_{\odot}} \right) \text{ erg s}^{-1}. \quad (27)$$

While this relationship is extremely uncertain (the normalization varies by a factor of two between M82 and NGC 253), it suggests that ULIRGs, or perhaps hyper-luminous infrared galaxies (HLIRGs, $L_{\text{IR}} > 10^{13} L_{\odot}$) may be sufficiently bright to contribute to the heating of the IGM.

While the fluxes from the brightest ULIRGs remain much smaller than those associated with the typical TeV blazars, there are many more starburst galaxies than AGN. At all redshifts ULIRGs constitute the high-luminosity tail of the star-forming galaxy luminosity functions (Le Floc'h et al. 2005; Caputi et al. 2007; Magnelli et al. 2009; Goto et al. 2010). In the present epoch, the density of ULIRGs is roughly $4 \times 10^{-7} \text{ Mpc}^{-3}$, and thus the corresponding VHEGR luminosity density of these objects, $\sim 2 \times 10^{34} \text{ erg s}^{-1} \text{ Mpc}^{-3}$ (see Table 8 of Caputi et al. 2007). is negligible in comparison to the TeV blazars, roughly $5 \times 10^{37} \text{ erg s}^{-1} \text{ Mpc}^{-3}$.

However, due to the steep decline of the luminosity function in the ULIRG range, small changes in the location of the break luminosity result in large changes in the comoving luminosity density of ULIRGs. As a consequence, the comoving luminosity density of ULIRGs grows much faster than that of quasars (and thus presumably the TeV blazars). Nevertheless, even at $z=2$, roughly the redshift of peak star formation, the comoving number density of ULIRGs remains below $\sim 2 \times 10^{-4} \text{ Mpc}^{-3}$ (see Table 8 of Caputi et al. 2007), corresponding to a comoving VHEGR luminosity density of $\lesssim 10^{37} \text{ erg s}^{-1} \text{ Mpc}^{-3}$, more than two orders of magnitude smaller than the contemporaneous TeV blazar population. For this reason, we neglect the starburst contribution to heating the IGM here, though they may represent an secondary source class.

3.4.2. Magnetars & X-ray Binaries

Stellar-mass objects, such as magnetars and X-ray binaries, generally have difficulty reaching the flux limits required for plasma cooling to dominate the pair beam evolution. Even at Eddington-limited VHEGR luminosities, reaching isotropic-equivalent luminosities of $10^{42} \text{ erg s}^{-1}$ requires beaming factors of roughly 10^4 , corresponding to jet opening angles of roughly 2° . In practice, the formation of radio jets is believed to be associated with substantially sub-Eddington accretion flows in these objects, and thus exacerbating the beaming requirement. More importantly, these sources may suffer compactness problems: the VHEGR emission regions in stellar-mass jets must necessarily be very far from the central object to avoid in situ pair-production. Finally, were X-ray binaries and magnetars generally strong, persistent VHEGR emitters with sufficiently large fluxes, we would expect that many would have been already detected.

3.4.3. Gamma-ray Bursts

Gamma-ray bursts (GRBs) are natural candidates due to their large luminosities and strong inferred beaming, and we consider them as a example of the general class of energetic transient sources. Unfortunately, little is known about the VHEGR emission of GRBs. Presently there is a single report of a TeV signal associated with a GRB (GRB 970417A, Atkins et al. 2000, 2003), though due to the large distances at which they can be observed and comparative rarity this is not unexpected. However, such high-energy emission is possible in principle, presumably due to inverse-Comptonization of the prompt emission and/or X-ray afterglow (see Section VIII of Piran 2004, and references therein). Fermi observations of GRBs have shown that for many events the Band spectrum can be extended to ~ 100 GeV (Abdo et al. 2009d,b,c; Ackermann et al. 2010), though in at least one case a spectral break below 10 GeV has been observed (GRB 090926A, Ackermann et al. 2011). Thus it remains unclear if in practice the high-energy emission is attenuated within the emission region. Moreover, since GRBs are inherently short-lived events, the luminosity limits described in Paper I, which require the VHEGR emitting phase to last for a plasma cooling timescale (roughly $10^2 \text{ yr} - 10^3 \text{ yr}$), are not directly applicable. A similar analysis, obtained by limiting the beam growth time to the GRB duration, gives VHEGR isotropic-equivalent energies of 10^{54} erg . This is comparable to the total prompt and afterglow emission for only the brightest bursts, comprising roughly 5% of GRBs observed by Swift (Gehrels et al. 2009). Nevertheless, even assuming that all GRBs produce the requisite high energy emission, at an optimistic present local rate of roughly $0.5 \text{ Gpc}^{-3} \text{ yr}^{-1}$, produces a comoving luminosity density of $\lesssim 10^{36} \text{ erg s}^{-1} \text{ Mpc}^{-3}$, roughly three orders of magnitude less than that due to TeV blazars at $z=1$.

4. THE THERMAL HISTORY OF THE IGM

The previous sections have shown that the VHEGR emission from luminous TeV blazars heats the IGM, quantified the magnitude and stochasticity of this heating locally, and estimated its evolution as a function of redshift. We are now in a position to discuss its impact on the thermal history of the IGM in detail. In the following we will show that TeV blazar heating can be substantial, dominating late time photoheating, and that its uniform nature naturally imprints its signature onto the temperature-density relation of the IGM.

The canonical history of the IGM is shaped by two important events: H reionization by the first stars at $z \sim 6\text{--}10$ and HeII reionization by quasars at $z \sim 3$ (see Furlanetto & Oh 2008, and references therein). Hydrogen and HeII reionization both heated the IGM to a $T \sim 2 \times 10^4 \text{ K} \text{--} 3 \times 10^4 \text{ K}$ or higher (in the case of HeII). Subsequently, the Universe cooled via adiabatic expansion, balanced by continuing photoheating due to ionization of recombining H. The entire canonical history of the IGM can thus be summarized as a competition between photoheating and adiabatic cooling, punctuated by intervals of sudden photoheating.¹¹

The addition of TeV blazar heating adds an additional extended heating component, and fundamentally alters the canonical picture for the thermal history of the IGM. In the following we explore the consequences of blazar heating using the one-zone model originally due to Hui & Gnedin (1997, hereafter HG97) (see also Hui & Haiman 2003). We begin by introducing this model in detail (Section 4.1), describe thermodynamic consequences of the new heating contribution from blazars and relate this to high- z Ly α measurements (Section 4.2), and close with a discussion of the implications for the local Ly α forest (Section 4.3).

4.1. One-Zone Model for the IGM

The thermal evolution of a fluid element in the IGM is governed by

$$\frac{dT}{dt} = -2HT + \frac{2T}{3(1+\delta)} \frac{d\delta}{dt} - \frac{T}{\Sigma \tilde{X}_i} \frac{d\Sigma \tilde{X}_i}{dt} + \frac{2}{3k_B n_{\text{bary}}} \frac{dQ}{dt}, \quad (28)$$

where H is the redshift dependent Hubble function, δ is the mass overdensity, $\tilde{X}_i = n_i/n_{\text{bary}}$ is the *proper* number fraction of species i , relative to the proper number density of baryons, $n_{\text{bary}} = \Omega_B \rho_{\text{cr}}/m_p$, ρ_{cr} is the critical mass density of the universe, and dQ/dt is the heating and cooling rate of the gas. The heating and cooling of IGM gas is governed by four processes: adiabatic cooling/heating from Hubble expansion/gravitational collapse, H/He photoionization heating, H/He recombination cooling, Compton cooling, and heating from TeV blazars. The evolution of the proper number fraction of the various species is given by

$$\frac{d\tilde{X}_i}{dt} = -\tilde{X}_i \Gamma_i + \sum_{j,k} n_{\text{bary}} \tilde{X}_j \tilde{X}_k R_{ijk}, \quad (29)$$

where the Γ_i are the associated atomic rates, not to be confused with the beam instability cooling rates discussed in Section 2. Finally, we demand a prescription for the density evolution, i.e., the evolution of δ . For this, we follow HG97 and assume the Zel'dovich approximation:

$$1 + \delta = \det^{-1} (\delta_{ij} + D_+ \psi_{ij}), \quad (30)$$

where D_+ is the linear growth factor (Peebles 1980). The 3×3 matrix, ψ , is determined by initial conditions. The exact form of this matrix is irrelevant. What is important, however, is the probability distribution of the eigenvalues of this matrix. For a Gaussian random field, the solution is known (Doroshkevich 1970); we use the formulation of Reisenegger & Miralda-Escude (1995).

Reionization of the Universe occurs in two stages: first H is reionized at some large redshift by stars and later He is

reionized around a redshift of $z \approx 3$ by quasars (see, e.g., Furlanetto & Oh 2008). To model this reionizing history, we adopt a sudden H photoionizing model (HG97):

$$J(z) = \begin{cases} J_0 & \text{for } z \leq z_{\text{reion}}, \\ 0 & \text{for } z > z_{\text{reion}}, \end{cases} \quad (31)$$

where z_{reion} is the redshift of H reionization and J_0 is the normalization of the reionizing radiation. While, this is not a realistic model of how H reionization occurs, its late time evolution (especially after $z \sim 3$) should be reasonably accurate. This is because the photoionizing background is observed to be roughly constants at these redshifts (Bolton et al. 2005; Becker et al. 2007; Faucher-Giguère et al. 2008) and the late time temperature asymptotes to a single value. This “loss of memory” of the specific reionization history in the evolution of the IGM is typical of reionization calculations (Hui & Haiman 2003).

To model the redshift dependence of H and He photoionization, we use the following spectral model for the radiation:

$$J_E(z) = J(z) \left(\frac{E}{E_{\text{HI}}} \right)^{-1.6} \begin{cases} 1 & \text{for } E \leq E_{\text{HeII}}, \\ 0.0 & \text{for } E > E_{\text{HeII}} \text{ \& } z > z_{\text{He}}, \\ 1.0 & \text{for } E > E_{\text{HeII}} \text{ \& } z < z_{\text{He}}, \end{cases} \quad (32)$$

where E is the energy of the photon, E_{HI} , E_{HeI} , E_{HeII} are the threshold energies corresponding to the ionization of HI, HeI, and HeII, $z_{\text{He}} = 3.5$ is the redshift of He reionization. The spectral index of -1.6 is typical of quasars and the spectral model of Equation (32) is similar to the He reionization model studied by Furlanetto & Oh (2008). Our model differs from theirs in that we ignore the density dependent effects of He reionization, i.e., that dense regions are reionized first. However, since we are interested solely in the magnitude of the effect of blazar heating, adopting this simplified model is justified.

The normalization of the photoionizing background in our model is fixed, determined by the H photoionizing rate:

$$\Gamma_{\text{HI}} = 4\pi \int_{E_{\text{HI}}}^{\infty} J_E \sigma_{\text{HI}} \frac{dE}{E}, \quad (33)$$

where σ_{HI} is the photoionizing cross section of HI. We choose the normalization of J_E to be $\Gamma_{\text{HI}} = 5 \times 10^{-13}$, which is inferred (with significant uncertainty) from the mean absorption of the Ly α forest (see for instance Bolton et al. 2005; Faucher-Giguère et al. 2008).

Equations (28–32) constitute a complete model for the evolution of a fluid element in the IGM. We numerically integrate these equations using a prescription for the heating and cooling microphysics specified in the Appendix of HG97. In Figure 7, we plot the evolution of the temperature for $\delta = 0$ patch with $z_{\text{reion}} = 19, 10$, and 6. The solid lines are the purely photoionized models without the effect of additional heating. For each of these models, we also set the redshift of HeII reionization at $z_{\text{HeII}} = 3.5$, which results in a temperature jump at that redshift. We note that at late redshift, the three different (purely photoionized) reionization histories asymptote to a single temperature evolution, highlighting the “loss of memory” property that is generic to photoionization-dominated models (Hui & Haiman 2003).

Generally, the thermal history of a given patch depends upon the particulars of the δ -evolution of the patch. In Figure 8 we show the temperature of ≈ 4000 realizations of an evolving patch as a scatter plot at a number of redshifts, ranging from $z = 0.5$ to $z = 4$. From this it is clear that the temperature-density relation is well approximated by a power law, consistent with

¹¹ We have ignored gravitational (shock) heating, which is progressively more important at densities larger than the mean density.

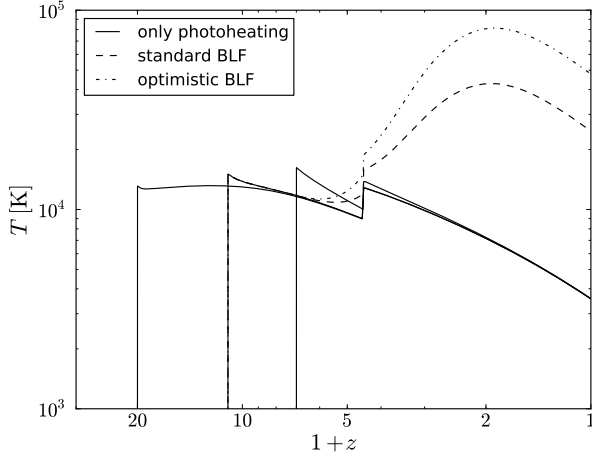


Figure 7. Thermal history of the a $\delta = 0$ patch of the IGM for the numerical solution (solid lines) of Equations (28), (29), and (30) using the prescription for the microphysics as specified in the Appendix of HG97. The solid curves are for sudden reionization histories for H and He (Equations (31) and (32)) for $z_{\text{reion}} = 19, 10$, and 6 and $z_{\text{HeII}} = 3.5$ going from left to right. The dashed (dashed-dotted) lines show the evolution using the blazar luminosity density, i.e., using the quasar luminosity density from (Hopkins et al. 2007) to normalize the local heating rate in our standard (optimistic) models (see Figure 10 and surrounding discussion).

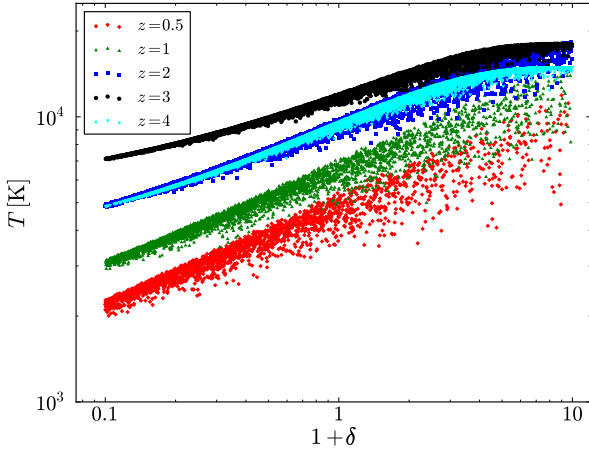


Figure 8. Temperature-density scatter plot for ≈ 4000 realizations at $z = 3$ (black dots), $z = 2$ (blue squares), $z = 1$ (green triangles), and $z = 0.5$ (red diamonds) when heating from TeV blazars is ignored. The shape of the temperature-density plot can be clearly be fit with a power law (with a positive index) and steadily falls from $z = 3.5$, i.e., after He reionization. The correspondence between the $z = 4$ and $z = 2$ points are simply an accident of choosing He II reionization at $z = 3.5$ and plotting the temperatures and densities at $z = 2$ and 4. Namely the Universe adiabatically cools, but the injection of heat at $z = 3.5$ resets the temperature and it proceeds cooling from that point onward.

those of HG97. Figure 8 represents a typical temperature-density relation, i.e., $T - \delta$ relationship, that is typical of most reionization calculations. Low density regions in the Universe are cooler compared to high-density regions due to decreased recombination (and hence photoheating) and a more rapid expansion (and hence greater adiabatic cooling). Missing from this simple picture are the effects of shocks and outflows from galaxies, i.e., feedback (see Davé et al. 2010 for instance). In addition, the temperature of the IGM is relatively cool ($\lesssim 10^4$

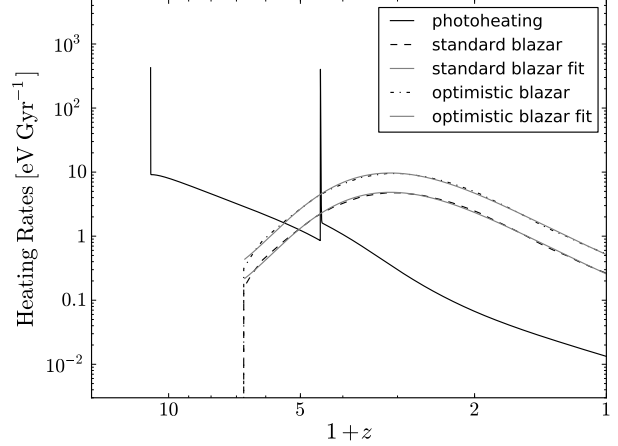


Figure 9. Photoheating (black solid line) and blazar heating rates for the standard (dashed line) and optimistic (dot-dashed line) as a function of redshift. The fits (eq.(38)) are denoted by gray lines for the standard and optimistic blazar heating models. We use a $\delta = 0$ fluid element in the IGM and calculate the amount of heat per baryon (in units of eV) per Gyr. The sharp jump at $z = 3.5$ is due to HeII reionization. Aside from this point, it is clear that blazar heating dominates the heating of the IGM. At late times $z \lesssim 2$, it is larger by over a factor of 10, though this is substantially greater for underdense regions.

K) for $\delta \lesssim 0$. This is because the temperature is suddenly raised to a few $\times 10^4$ K after H and He reionization, but rapidly cools due to the effects of adiabatic expansion. These generic characteristics are typical of most reionization models and are expected following the arguments of HG97 and Hui & Haiman (2003).

4.2. Contribution of TeV Blazar Heating

When the effects of heating due to the VHEGR emission from blazars are included, the properties of the IGM are substantially altered. The consequence of TeV blazar emission is shown for a $\delta = 0$ patch of the IGM by the dashed line in Figure 7. The thermal history begins to deviate significantly from that due to photonization and adiabatic expansion alone by $z \simeq 6$, becomes dominant near $z \simeq 3$, and peaks at roughly $4 - 8 \times 10^4$ K at $z \simeq 1$ before the rapid decline in $\Lambda_B(z)$ combined with adiabatic cooling causes the temperature to fall off (the range corresponds to the uncertainty in estimating the number of blazars contributing to the heating rate). Thus, it is clear that heating by blazars is significant, dominates at low redshifts (following He reionization), and potentially dominates the thermal evolution of the IGM in low-density regions.

The effect of TeV blazar heating qualitatively changes the picture of the IGM. First, the temperature-density relation is inverted with the low-density regions being the hottest. Second, the overall temperature of the IGM is significantly hotter. The reasons for both of these are twofold. First, TeV blazars are a substantial reservoir of heating, potentially increasing the IGM temperature by a few $\times 10^4$ K, and dominating the contribution from ionizing photons for $1 + \delta \lesssim 10$. Second, the heating rate is nearly independent of density, depending most strongly upon the number density of TeV blazars and the number density of UV photons, both of which are nearly uniform (though see Section 3.2). The effect of a uniform heating rate is that the energy deposited per baryon is substantially larger in more tenuous regions of the Universe, with underdense regions experiencing larger temperature increases as a result.

The dominance of TeV blazar heating over photoheating is shown explicitly in Figure 9, where the blazar heating rate (dashed line) is compared to the photoheating rate (solid lines) as a function of redshift for a $\delta = 0$ patch of the IGM. At $z = 3.5$, there is a sudden jump in the photoheating rate due to nearly instantaneous HeII reionization. Following HeII reionization, the blazar heating rate is about an order of magnitude larger than that due to photoheating¹². Because the photoheating rate is $\propto (1 + \delta)$, the dominance of TeV blazar heating is even more apparent at lower densities.

The contribution of TeV blazar heating to the thermodynamics of the IGM for the standard model appears to be significant around the period of HeII reionization. In our model, this is partially a result of our sudden reionization prescription for HeII reionization at $z = 3.5$. However, we can also show with the following order-of-magnitude calculation that the effect of TeV blazar heating must begin to be important around the era of He II reionization that has been observationally constrained to be around $z \sim 3$.

To begin we first show that He reionization finishes around $z \approx 3$. The comoving number density of He is

$$n_{\text{He}} = f_{\text{He}} \frac{\Omega_B \rho_{\text{cr}}}{A_{\text{He}} m_p} \approx 1.5 \times 10^{-8} \text{ cm}^{-3}, \quad (34)$$

where $f_{\text{He}} = 0.24$ and $A_{\text{He}} = 4$ are the primordial mass fraction and the atomic number of He, respectively. To estimate the comoving density of HeII ionizing photons at $z \sim 3$, we note that the 1 Ry photon comoving density at $z = 3.5$ from quasars in the Hopkins et al. (2007) QLF is $\dot{n}_{1\text{Ry}} \approx 5 \times 10^{-7} \text{ cm}^{-3} \text{ Gyr}^{-1}$ (e.g. see Figure 9 of Hopkins et al. 2007). As the spectral index of quasars is -1.6 , this implies that comoving number density of ionizing HeII photons is $\dot{n}_{4\text{Ry}} \approx 5 \times 10^{-8} \text{ cm}^{-3} \text{ Gyr}^{-1}$. Thus, the total comoving density of HeII ionizing photons produced at $z = 3.5$ is

$$n_{4\text{Ry}} \sim \frac{\dot{n}_{4\text{Ry}}}{H(z = 3.5)} \approx 10^{-7} \text{ cm}^{-3}. \quad (35)$$

Before we compare of equation (35) with (34), we note the it takes roughly 2-3 He ionizing photons to completely ionize He and that obscuring material around a quasar will remove half of the ionizing flux (McQuinn et al. 2009). With these efficiency factors in mind, the comoving density of HeII ionizing photons at $z \sim 3$ is just large enough to reionize HeII.

The amount of excess energy per HeII ionization is 16 eV for an ionizing radiation spectral index of -1.6 . Given that there are ≈ 3 ionizing photons per HeII reionization, the excess energy dumped into the IGM during HeII reionization is

$$\mathcal{Q}_{\text{exc,HeII}} = \epsilon_{\text{exc,HeII}} \frac{f_{\text{He}} \Omega_B \rho_{\text{cr}}}{A_{\text{He}} m_p} \approx 6 \times 10^{-7} \text{ eV cm}^{-3}, \quad (36)$$

where $\epsilon_{\text{exc,HeII}} = 48 \text{ eV}$ is the average excess energy dumped per HeII ionization, $f_{\text{He}} = 0.24$ is the primordial mass fraction of He, and $A_{\text{HeII}} = 4$ is the atomic number of He. To compare this to the energy dumped from TeV blazars, we start with the comoving luminosity density of blazars at $z = 3.5$ is $\Lambda_B(z = 3.5) \approx 3 \times 10^{38} \text{ erg s}^{-1} \text{ Mpc}^{-3}$, which we estimate from Figure 3. Over a Hubble time at $z = 3.5$, the amount of energy dumped

into the IGM by TeV blazars per comoving volume is then

$$\mathcal{Q}_B|_{z=3.5} = \frac{\Lambda_B(z = 3.5)}{H(z = 3.5)} \approx 5 \times 10^{-7} \text{ eV cm}^{-3}, \quad (37)$$

which compares favorably with Equation (36) and shows that as HeII reionization is being completed, the effect of blazar heating begins to be pronounced.

For convenience, we provide a fitted third-order polynomial formula for our estimated *proper* blazar heating rate for $z \leq 5.7$:

$$\log_{10} \left(\frac{\dot{\mathcal{Q}}_B / n_{\text{bary}}}{1 \text{ eV Gyr}^{-1}} \right) = 0.0315(1+z)^3 - 0.512(1+z)^2 + 2.27(1+z) - \log_{10} \dot{\mathcal{Q}}_{\text{mod}} \quad (38)$$

Here, $\log_{10} \dot{\mathcal{Q}}_{\text{mod}} = \{2.38, 2.08\}$ for the “standard” and “optimistic” (see below) blazar heating model, respectively. The fits are shown by the solid (gray) lines in Figure 9. Note that we have calculated the heating rate as a heating rate per baryon, i.e., $\dot{\mathcal{Q}}/n_{\text{bary}}$, so that it is independent of the ionization fraction.

The effect of blazar heating upon the void temperature-density relation is shown in the left panels of Figure 10 for the “standard” (upper) and “optimistic” (lower) heating models. In comparison to the case in which blazar heating is neglected (Fig. 8), the voids are hotter at all redshifts. Overall, the IGM never drops below 10^4 K , with low-density regions remaining substantially hotter than this. By contrast, the temperature of the IGM without blazar heating does not *exceed* 10^4 K (Fig. 8). In these low-density regions the temperature can exceed 10^5 K with TeV blazar heating, almost two orders of magnitude hotter than anticipated by photoheating and adiabatic cooling alone. To show this result more clearly, we show in the right panels of Figure 10 the ratio between the temperature for a photoheating only model (T_{photo}) and for a model including blazar heating (T_{blazar}) for the “standard” (upper) and “optimistic” (lower) heating models. This shows that the temperature in low-density patches in the Universe, i.e., small $1 + \delta$, increase by a factor of ~ 100 and ~ 200 for the “standard” and “optimistic” heating models, respectively.

Figure 10 shows that blazar heating qualitatively changes the IGM temperature-density relation. In particular, the IGM temperature-density relation is inverted for $\delta \lesssim 0$. This compares favorably with recent evidence for just such an inverted temperature-density relation (Bolton et al. 2008; Viel et al. 2009). Notably, in the lower panel of Figure 10 we plot as a solid (gray) line the temperature-density relation $T = 2.4 \times 10^4 (1 + \delta)^{-0.49} \text{ K}$, inferred at $z = 3$ empirically by Viel et al. (2009). Here to produce a better match to the empirical measurements of Viel et al. (2009), we introduce the “optimistic” heating model, i.e., we choose a value of the remaining coefficient of the sky incompleteness correction for TeV blazars of $\eta_{\text{sys}} = 1.6$, which includes variations of the TeV blazar redshift evolution, additional TeV sources that may contribute to the plasma instability heating, and potentially spectral variability. As a result, the local heating rate is enhanced over the “standard” heating rate by a factor of two or $\dot{\mathcal{Q}}|_{z=0} \approx 1.4 \times 10^{-7} \text{ eV cm}^{-3} \text{ Gyr}^{-1}$. The match produced between the empirical relation of Viel et al. (2009) and our “optimistic” TeV blazar model is striking in that it matches the slope in the absence of any tuning as well as the normalization within the uncertainties of our estimated incompleteness correction (see Figure 3). This inversion of the temperature-density relation is difficult to

¹² Prior to HeII reionization, the photoionization and blazar heating rates are inconsistent due to the artificial ionizing photon distribution assumed in Equation 32. Specifically, for reasons of simplicity, we have ignored the ionizing photons produced by the quasars. Following HeII reionization, however, this is no longer an issue.

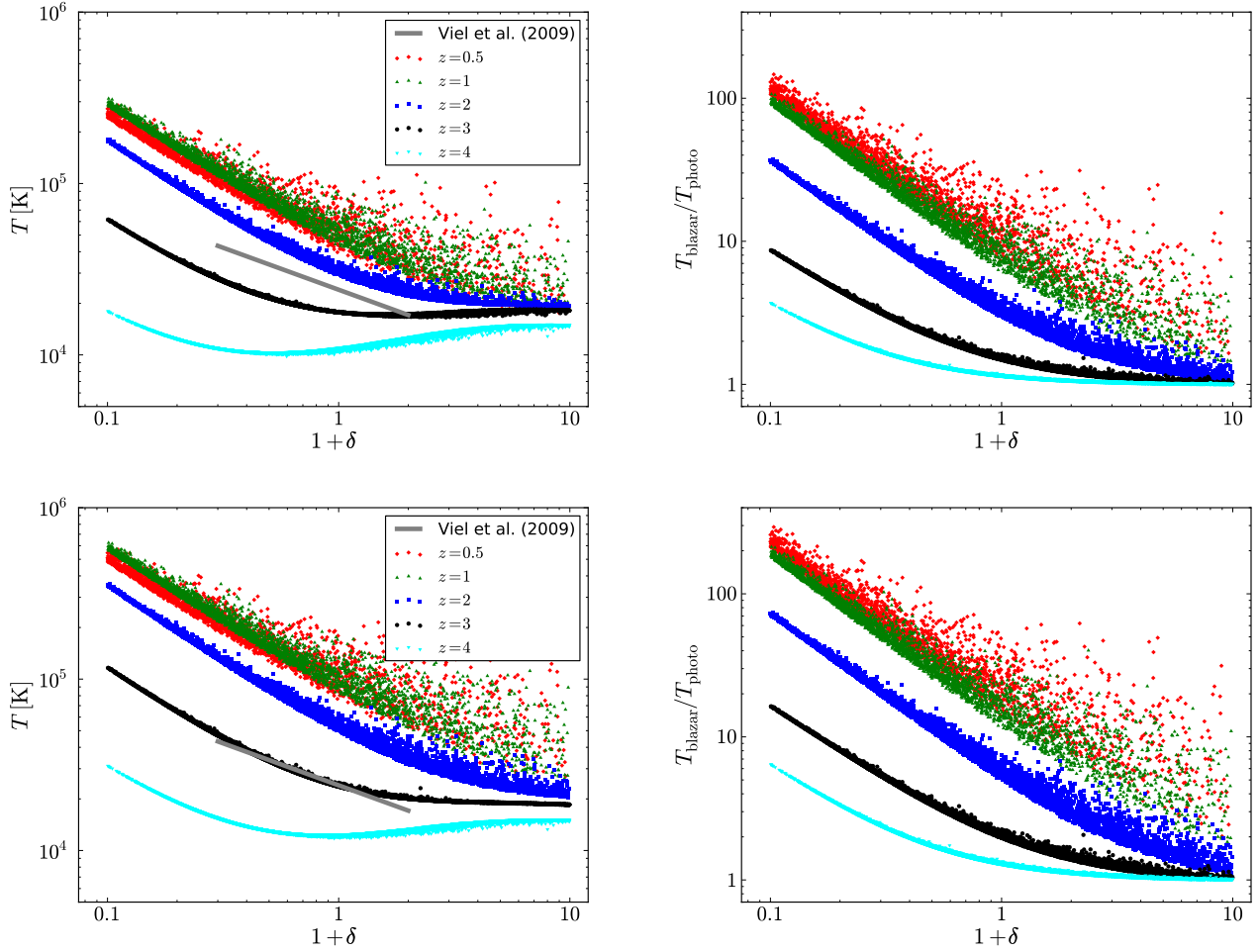


Figure 10. Temperature-density scatter plots (left panels; same as Figure 8) including the effects of blazar heating for our standard (top) and optimistic (bottom) heating models. The right panels show the ratio between including only the effects of photoheating (T_{photo}) and including the effects of blazar heating (T_{blazar}) for the same realization for the standard (top) and optimistic (bottom) blazar heating models. Note for the left panels that the temperature evolution due to blazar heating is qualitatively different from the earlier case (Fig. 8). Starting at $z = 4$, the temperature-density relation in the lowest density regions of the Universe is inverted. This inverted temperature relation moves to higher densities with decreasing redshift until at $z = 0.5$, it goes down to $\delta \approx 2$. The IGM temperature is also significantly hotter, with the hottest regions having $T > 10^5$ K. Overplotted is the observational determined temperature-density relation at $z = 3$ (solid gray line) from (Viel et al. 2009). The right panels show that the temperature increases by a factor of ~ 100 (standard heating) and ~ 200 (optimistic heating) for small $1 + \delta$ patches of the Universe when the effects of blazar heating are taken into account.

reproduce using HeII reionization alone (McQuinn et al. 2009; Bolton & Becker 2009) though is a natural consequence of TeV blazar emission.

Energetically, the magnitude of the impact from TeV blazars in low-density regions is somewhat surprising. The radiative output from stars and quasars far outstrips that from VHEGR sources, yet in practice the heating rate from blazars is much larger. This is because the photoheating rate is ultimately limited by the HII recombination rate. Indeed, this is precisely the property invoked to show that the effect of the epochs of H and HeII reionization is washed out at low redshift, unless these occurred recently (Hui & Haiman 2003).

By contrast no such limitation exists for TeV blazars, paving the way for them to dominate the heating of the low-redshift Universe, a point that we have made already in the Introduction. Instead, the VHEGR emission from blazars is deposited in the IGM with order unity efficiency. The rate of heating in this case depends linearly on the radiative output of these TeV blazars, and is independent of the atomic physics of the IGM. In addition these sources have a constant heating rate per unit

volume (whereas photoheating heats per unit mass). Hence, the effect of blazar heating, which is already pronounced, is amplified relative to photoheating in low-density regions, leading to an inverted temperature-density relation. Therefore, not only is the memory of photoheating erased in low-density regions, but it is overwritten by the record of blazar heating.

Following this work, we have recently completed a study of the effects of blazar heating in a more detailed hydrodynamic model of structure formation, reported in a follow-up paper (Puchwein et al. 2011). Using the blazar heating prescription given by equation (38), we show that the optical depth of the Ly α forest is reproduced using a H photoionization rate of $\Gamma_{\text{HI}} \approx 5 \times 10^{-13} \text{ s}^{-1}$ or equivalently using the inferred ionizing background from (Faucher-Giguère et al. 2009). We also confirm that the low density IGM again possesses an inverted temperature-density relation (as shown in Figure 10). In addition, a detailed comparison between the results of our numerical calculations and observations show that a blazar heated universe matches the one- and two- points statistics of the high

redshift Ly α forest, but also matches the line width distribution. This excellent agreement was achieved using the best estimate on the evolution of the photoionizing background (without tuning) and is due to the excess energy injection into the low density IGM.

4.3. Implications for the local Ly α forest

While TeV blazar heating can with significant success reproduce some of the peculiar properties of recent high- z Ly α observations, the most dramatic departures from the IGM thermal history in the absence of blazar heating occur at $z \lesssim 1$. This is a result of the relatively recent nature of quasar activity and the cumulative effect of blazar heating. Thus we might anticipate dramatic consequences for the local Ly α forest, potentially in conflict with studies of nearby Ly α clouds (e.g., Penton et al. 2000b,a, 2002, 2004; Davé et al. 2010). However, this does not occur due to the physical nature of the clouds that produce the local Ly α forest.

The structures responsible for the local Ly α forest are almost certainly associated with significant overdensities as suggested by large-scale hydrodynamic computations (e.g., Davé et al. 2010)¹³. These simulated Ly α forest calculations provide a means to relate the empirically inferred HI columns to the properties of the dynamical structures responsible for the Ly α clouds. For HI columns of 10^{13} – 10^{14} cm $^{-2}$, the lowest values for which Ly α measurements exist, the simulations find that the local Ly α forest is produced primarily by the intergalactic filaments, corresponding to $1+\delta \gtrsim 5$ –500 (e.g., see the bottom-left panel of Figure 8 and Figure 9 of Davé et al. 2010).

We emphasize this point with the following order-of-magnitude estimate. An upper limit upon cloud sizes can be obtained using the line widths, b , translating into a proper size of $1.4(b/10^2 \text{ km s}^{-1}) \text{ Mpc}$ (Penton et al. 2000a). A lower limit upon the local ionizing background can be inferred from the optical depth of VHEGRs, giving $\sim 10^{-6} \text{ erg s}^{-1} \text{ cm}^{-2} \text{ sr}^{-1}$ (Aharonian et al. 2006a). Employing ionization balance to set the HI fraction, for $z < 1$ this gives the column densities $\lesssim 3 \times 10^{10} (1+\delta)^2 (1+z)^{6-\zeta} (T/10^4 \text{ K})^{-0.65}$ for $T < 10^5 \text{ K}$. From this it is clear that the nearby Ly α clouds must correspond to regions with $1+\delta \gg 1$.¹⁴

At these overdensities, the impact of blazar heating on their thermal history is modest at best. By $1+\delta = 5$ the blazars change the IGM temperature by a factor of 2, raising it to roughly $4 \times 10^4 \text{ K}$, comparable to the temperatures typical of the local Ly α clouds (Davé et al. 2010). At $1+\delta > 50$ blazar heating is negligible in comparison to photoionization and shock-heating. Thus, because low- z Ly α absorbers are biased toward high-density regions, they serve a poor probe of low-density regions and are unaffected by the effects of TeV blazars.

The inclusion of blazar heating into these large-scale hydrodynamic calculations is an important next step. However, we do not expect a significant impact on the local Ly α forest. A more important impact of TeV blazar heating would be on the formation of collapsed structures, which is a topic that we will explore in Paper III.

4.4. Limits on the direct detection of the hot IGM

¹³ We note in passing, that for $z \gtrsim 2$, the same simulations imply that Ly α forest contains significant contributions from regions with $1+\delta \sim 1$.

¹⁴ Note, however, that since the column density is $\propto (1+z)^6$ at $z > 1$, we would nevertheless expect low-density regions to contribute significantly to the high- z Ly α forest, as has indeed been found to be the case.

As low-density regions are immune to local Ly α probes, we now turn to the question whether there are methods of directly inferring the presence of such high temperatures in these regions. First, we compute the mean Comptonization of the CMB due to blazar heating,

$$\langle y \rangle = \sigma_T \int_0^{h_{\text{HI}}} dD \frac{\langle n_e k (T_e - T_{\text{CMB}}) \rangle}{m_e c^2}, \quad (39)$$

where n_e is the free electron density. Here, n_e is the physical density of free electrons and we integrate along the proper distance of the photons back to recombination, $dD = -c da a^{-1} = -c da (aH)^{-1}$ where the minus sign arises due to the choice of coordinates which are centered on the observer. Performing the integral with our temperature evolutions at mean density (i.e. neglecting gravitational heating by formation shocks) yields mean Comptonization values of $\langle y \rangle = \{1.4, 1.9, 2.5\} \times 10^{-7}$ for our models without blazar heating and those with standard and optimistic blazar heating. To date the best limits on the mean Comptonization come from the COsmic Background Explorer Far-InfraRed Absolute Spectrophotometer experiment (COBE FIRAS) which measure the difference between the CMB and a perfect black-body spectrum (Fixsen et al. 1996). Their upper limit of $|y| < 1.5 \times 10^{-5}$ (95% confidence level) is perfectly consistent with our inferred mean Comptonizations. With current technology, it appears to be quite feasible to measure the deviation of the CMB spectrum from a perfect blackbody form with an accuracy and precision of 1 ppm yielding constraints on the cosmic y -parameter at the level of 10^{-7} and provide a spectrum of the anisotropy to 10% (Fixsen & Mather 2002). We note, however, that the mean Comptonization is expected to be dominated by gravitational heating which leads to values of $\langle y \rangle = 2.6 \times 10^{-6}$ inferred from cosmological simulations by Springel et al. (2001). The mean temperature of these cosmological simulations of $\langle T_0 \rangle = 0.3 \text{ keV}$ suggests that the signal is dominated by collapsed galaxy groups and unvirialized infall regions onto galaxy clusters that constitute the hot component of the warm-hot intergalactic medium. Hence, in order to measure the blazar heating signal in the mean Comptonization of the CMB, the fluctuating part due to gravitational heating would have to be subtracted first. Since galaxy groups dominate the fluctuation power on angular scales of $< 5'$, the measurement of the deviation of the CMB spectrum would have to be performed on these small angular scales which appears to be difficult.

Second, we estimate the emission of the IGM due to free-free emission (bremsstrahlung) and synchrotron emission. Turning to the question of synchrotron emission, we estimate the synchrotron frequency using a maximal IGMF strength of $B \sim 10^{-9} \text{ G}$. At temperatures of $\sim 10^4$ – 10^5 K , the electrons in the IGM are nonrelativistic. Hence the synchrotron frequency is roughly the Larmor frequency, $\omega_{\text{sync}} \approx \omega_G = eB/m_e c \approx 2 \times 10^{-2} (B/10^{-9} \text{ G}) \text{ s}^{-1}$. These low frequencies are well below the plasma frequency of the IGM, $\omega_p = \sqrt{4\pi e^2 n_e / m_e} \approx 25 \text{ Hz}$ and, hence, will be absorbed by the IGM. Free-free emission from the IGM can cause a distortion in the CMB at low frequencies (Bartlett & Stebbins 1991). As the free-free emissivity scales like $\propto n_e^2 T^{-0.35}$ for fully ionized primordial gas, it scales weakly with temperature but strongly with clumpiness. As a result, overdense haloes dominate free-free emission, with the contribution from low density IGM being 1-3 orders of magnitude smaller (Oh 1999; Cooray & Furlanetto 2004; Ponente et al. 2011). The effect of blazar heating will

further suppress this free-free emission (albeit mildly) from the IGM compared to that of overdense halos. Finally, the best constraints on this free-free optical depth of $\tau_{\text{ff}} < 1.9 \times 10^{-5}$ (Bersanelli et al. 1994) is still too large compared to optimistic models of free-free emission from overdense haloes by at least an order of magnitude and by ≈ 3 orders of magnitude from the smooth IGM (Cooray & Furlanetto 2004; Ponente et al. 2011).

5. MEASURING THE HIGH-ENERGY LUMINOSITY OF BLAZARS

Thus far, we have concerned ourselves with the impact of TeV blazars on the Universe at large. In this section, we invert this argument and discuss how the Universe at large can be used as a probe of the physics of VHEGR photons and the global properties of TeV blazars. Namely, the estimated heating rates used in this paper – standard and optimistic – suffer from a number of uncertainties, including statistical fluctuations in the number of presently observed VHEGR sources, the redshift evolution of the TeV blazar luminosity density, and the detailed form of the VHEGR and EBL spectra. However, due to the high efficiency with which the VHEGR luminosity of blazars is converted to heat within cosmic voids, the temperature history of the voids themselves provides a way to determine the cumulative TeV blazar luminosity density empirically.

This is possible due to a number of fortuitous properties of voids and TeV blazar heating. First, the high efficiency with which the VHEGR emission of blazars is converted to heat implies that even in voids the Universe acts as a calorimeter. Second, blazar heating dominates the thermal history of voids for $z \lesssim 4$ (see, e.g., Figure 9) so that this calorimeter is uncontaminated. We caution that HeII reionization complicates matters somewhat, though in our model makes a comparatively small correction to the temperature evolution of low-density regions (see Figure 7). However, this depends upon the particular manner in which HeII reionization occurred, and could in principle provide a somewhat larger contribution in inhomogeneous reionization scenarios (see Section 3 of Furlanetto & Oh 2008, for a detailed discussion). Finally, within voids the adiabatic losses to Hubble expansion are very accurately modeled in the linear regime, substantially simplifying the interpretation of void temperature histories.

Perhaps the greatest uncertainty is the physics of the mechanism which converts pair beams from TeV blazars to thermal energy in the IGM. In the context of the "oblique" instability, what is unclear is the luminosity cutoff of TeV blazars probed in this manner, which arises from the competition between inverse-Compton and plasma processes. If this cutoff may be conservatively assumed to lie at an isotropic-equivalent $EL_E \simeq 10^{42} \text{ erg s}^{-1}$, corresponding to a true luminosity 2–3 orders of magnitude lower due to the presumed jet beaming, then this is dimmer than all but two of the TeV blazars known. Assuming that the TeV blazar luminosity function follows that of quasars, the luminosity density is dominated by sources near the break luminosity, and thus as long as the lower-luminosity cutoff is sufficiently low (below that of the break luminosity) it may be neglected. For the TeV blazars listed in Table 1, this break occurs near $3 \times 10^{44} \text{ erg s}^{-1}$, and thus is well above the relevant cutoff. Measurements of the thermal history of voids directly corresponds to the TeV blazar bolometric luminosity evolution. In this manner, the thermal history of cosmic voids provides an analogous argument to that by Soltan (1982) for determining the blazar luminosity density, $\Lambda_B(z)$. Such a constraint on the history of $\Lambda_B(z)$ can be used to study the history

of accretion in the Universe and the jet forming efficiency by comparing it to the history quasar or active galaxy luminosity density. While probes of the low-density IGM at low redshift are sparse, the situation at $z \sim 2-4$ is much more hopeful as we have discussed in Section 4.2. Thus, precision measurements of the Ly α forest at $z \sim 2-4$ (e.g. Viel et al. 2009) alongside detailed studies of HeII reionization (McQuinn et al. 2009, e.g.) offer the best constraint both on the fate of VHEGR photons and the evolution of TeV blazars, i.e., the blazar luminosity density.

6. CONCLUSIONS

In this work, we have explored the effect of TeV blazar heating on the thermal history of the IGM. We have argued that VHEGRs that are sufficiently hard to pair produce off of the EBL, will inevitably dump the majority of their energy into the IGM via plasma instabilities. By collating the nearby 28 TeV blazars with firm spectral measurements, we have determined the local observed heating rate after correcting for the various selection effects using *Fermi* observations of TeV blazars. This local heating rate of $\dot{Q} = 7 \times 10^{-8} \text{ eV cm}^{-3} \text{ Gyr}^{-1}$, which we call the standard model, can be extended to higher redshift by normalizing it to the Hopkins et al. (2007) quasar luminosity density. This follows from the important result of Paper I, which shows that the local observed blazar luminosity function is well in line with the local quasar luminosity function corrected by a factor of $\approx 10^{-3}$. This TeV blazar heating should be relatively homogeneous at all redshifts $z \lesssim 4$ with greater spatial variations for at higher z , approaching order unity at $z \sim 6$.

This redshift dependent blazar heating is substantial and is larger than the photoheating rate by a factor of 15 (standard) - 30 (optimistic) after He reionization for a $\delta = 0$ patch of the Universe. Using a simple one-zone model of the IGM, we demonstrate that the effect of including TeV blazar heating versus not including TeV blazar heating leads to qualitative and quantitative changes in the thermal history of the IGM. First, the injection of heat into the IGM by blazars substantially increases the temperature of the IGM. In the case with blazar heating, the temperature of the IGM stays above 10^4 K , with some regions approaching 10^6 K , whereas without blazar heating, the temperature of the IGM tends to stay below 10^4 K .¹⁵ Second, the even volumetric heating rate of blazars impacts the thermal history of low-density regions much more strongly than higher density regions. Low-density regions are substantially hotter as a result with temperatures in excess of $\gtrsim 10^5 \text{ K}$. Higher density regions on the other hand are not heated as much by blazars. This naturally produces an inverted temperature-density relation which matches the empirical results of Viel et al. (2009) if we increase the amount of blazar heating, i.e., the optimistic model, to $\dot{Q} = 1.4 \times 10^{-7} \text{ eV cm}^{-3} \text{ Gyr}^{-1}$. It also provides an encouraging endorsement of our model as such inverted temperature-density relations are difficult to produce in standard reionization histories. We have demonstrated these salient points more explicitly in a follow up paper (Puchwein et al. 2011), where we calculate the effect of blazar heating in a hydrodynamic realization of the universe. We show that the comparison between a blazar heated universe and observation of the high redshift Ly α forest gives excellent quantitative agreement.

As our model predicts a substantially hotter low-density IGM

¹⁵ Again, we have ignored the effects of gravitational (shock) heating which is important at densities above mean density.

that standard models predict, we then proceeded to investigate either if this model breaks current constraints on the local temperature of the IGM or can be directly measured. Unfortunately, the local Ly α forest is an ineffective probe of this environment compared to the high- z Ly α forest as the regions that give rise to the local Ly α forest are dense regions that remain relatively unaffected by the effects of blazar heating. Other means of directly probing this hot IGM via Comptonization of the CMB and free-free emission are also unlikely.

Finally, we note that the thermodynamics of the IGM can be used as a calorimeter for VHEGR emission of blazars in the Universe. Namely, because the low-density IGM is so sensitive to the total amount of energy dumped into it, which is dominated by TeV blazars, we argue that the thermal history of the low-density IGM can be used to measure the total energy output in VHEGRs over cosmic time. In principle, this would allow a determination of the blazar luminosity density as a function of redshift, as well as constrain the history and physics of accretion onto supermassive black holes, i.e., rates of radiative versus radiatively inefficient accretion and jet formation efficiency. However, the contaminating effects of He II reionization would have to be explored in detail before such physics can be elucidated.

We thank Tom Abel, Marco Ajello, Marcelo Alvarez, Arif Babul, Roger Blandford, James Bolton, Mike Boylan-Kolchin, Luigi Costamante, Andrei Gruzinov, Peter Goldreich, Martin Haehnelt, Andrey Kravtsov, Ue-li Pen, Ewald Puchwein, Volker Springel, Chris Thompson, Matteo Viel, Marc Voit, and Risa Wechsler for useful discussions. We also thank the referee, David Weinberg, for a thorough reading of the manuscript and for his constructive comments. We are indebted to Peng Oh for his encouragement and useful suggestions. We thank Steve Furlanetto for kindly providing technical expertise. These computations were performed on the Sunnyvale cluster at CITA. A.E.B. and P.C. are supported by CITA. A.E.B. gratefully acknowledges the support of the Beatrice D. Tremaine Fellowship. C.P. gratefully acknowledges financial support of the Klaus Tschira Foundation and would furthermore like to thank KITP for their hospitality during the galaxy cluster workshop. This research was supported in part by the National Science Foundation under Grant No. NSF PHY05-51164.

APPENDIX

A. DEFINING THE NUMBER OF BRIGHT BLAZARS

Here we provide a more detailed discussion of how “likely” it is for a patch of the Universe at a given redshift to experience a large deviation from the average TeV blazar heating rate. We will pursue this primarily by attempting to compute the “number of blazars a patch sees” as a function of redshift, $\mathcal{N}_B(z)$. This is, however, a poorly defined quantity, the primary difficulty being the determination of which objects to count. In principle, we would like to take a census of those sources “responsible for the bulk of the heating”; in practice this is an ambiguous definition. Thus, here we will describe and contrast a number of possible definitions. In the process, we will also elucidate which objects dominate the heating.

A.1. Preliminary Definitions and Assumptions

In the interest of completeness we will forgo the assumption that the heating is local, and perform the appropriate cosmological calculations. However, since we ultimately would like

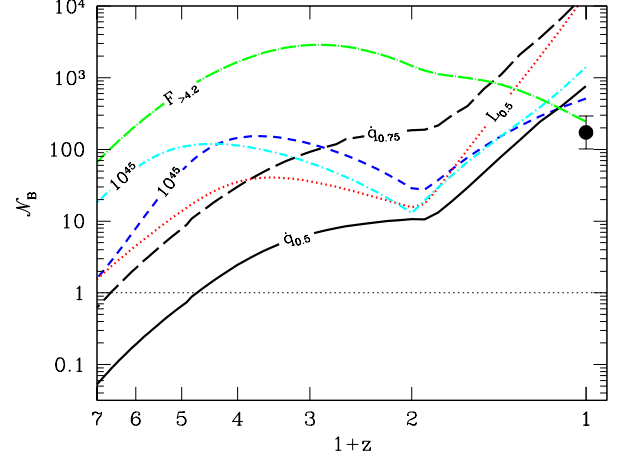


Figure 11. Same as Figure 5 with the addition of the cyan, short-dash-dotted line, showing the instantaneous number of blazars within a comoving volume of radius $(1+z)\bar{D}_{pp}$, and the green, long-dash-dotted line, showing the number of blazars seen at a particular redshift above a flux limit of $4 \times 10^{-12} \text{ erg cm}^{-2} \text{ s}^{-1}$, roughly that inferred from the very-high energy gamma-ray observations. The remaining lines are as defined in Figure 5: The blue, short-dashed line shows the instantaneous number of blazars with intrinsic isotropic-equivalent luminosities above $10^{45} \text{ erg s}^{-1}$ within the $\bar{\tau} = 1$ surface, the red, dotted line shows the number of blazars above the median luminosity at each redshift within the $\bar{\tau} = 1$ surface, and the black, solid (long-dashed) line shows the number of blazars with individual heating rates that exceed that above which half (0.75 times) of the heating is produced. For reference, our estimate of the sky-completeness corrected number of TeV blazars *observed in the TeV* is shown by the black circle, with the error bars denoting the Poisson uncertainty only. Note that for all calculations we have assumed $L_M = 2 \times 10^{46} \text{ erg s}^{-1}$ and adopted $\alpha = 3$.

to identify \mathcal{N}_B as a function of observer redshift, z_o , we require observed-dependent definitions of the standard complement of cosmological distances. Specifically, we use the following generalizations of the standard proper, angular diameter, and luminosity distances,

$$\begin{aligned} D_P(z; z_o) &= D_P(z) - D_P(z_o) \\ D_A(z; z_o) &= \frac{D_C(z) - D_C(z_o)}{1+z} \\ D_L(z; z_o) &= (1+z) \frac{D_C(z) - D_C(z_o)}{(1+z_o)^2}, \end{aligned} \quad (\text{A1})$$

where $D_C(z)$ and $D_P(z)$ correspond to the $z = 0$ comoving and proper distances, respectively. Note that these reduce to their expected expressions when $z_o = 0$.

While we have already defined the mean free path of high-energy gamma rays in Equation (3), we also require a definition of the optical depth that a gamma ray that originates at z with *observed* energy E at z_o accrues during its propagation:

$$\tau(E, z; z_o) = \int_{z_o}^z \frac{1}{D_{pp}[(1+z)E/(1+z_o), z]} \frac{dD_P}{dz} dz. \quad (\text{A2})$$

As with $\tau(E, z)$, this differs from the definition of $\tau_E(E, z)$ at $z_o = 0$ given in Paper I, where there we set E to the *emitted* energy of the gamma ray.

We define the flux, $F(E_m, E_M)$, to be that integrated between a given energy range, E_m to E_M (usually 100 GeV to 10 TeV),

$$F(E_m, E_M) = \int_{E_m}^{E_M} dE F_E = f_0 E_0^\alpha \int_{E_m}^{E_M} E^{1-\alpha} dE, \quad (\text{A3})$$

where the observed photon number flux is given by Equation

(12). For a source at redshift z , this corresponds to an absorption corrected flux of

$$\bar{F}(z; z_o, E_m, E_M) = \int_{E_m}^{E_M} dE F_E e^{-\tau(E; z; z_o)}, \quad (\text{A4})$$

and therefore an intrinsic luminosity between energies $E_m(1+z)/(1+z_o)$ and $E_M(1+z)/(1+z_o)$ of $L(z; z_o, E'_m, E'_M) = 4\pi D_L^2(z; z_o)^2 \bar{F}(z; z_o, E_m, E_M)$ where E'_m and E'_M are the energies bounding the relevant range at z . Since we would like to compare luminosities within a band across redshifts (i.e., keep E_m and E_M fixed), we must correct for the fixed spectral shift induced by the different redshifts. Assuming that the spectrum is a power law (as we shall do in all cases here), this implies an additional redshift factor:

$$\begin{aligned} L(z; z_o, E_m, E_M) &= 4\pi \left(\frac{1+z}{1+z_o} \right)^{\alpha-2} D_L^2(z; z_o) \bar{F}(z; z_o, E_m, E_M) \\ &= 4\pi \left(\frac{1+z}{1+z_o} \right)^{\alpha-2} D_L^2(z; z_o) e^{-\bar{\tau}} F(E_m, E_M), \end{aligned} \quad (\text{A5})$$

where $\bar{\tau}$ is the spectrally average optical depth:

$$\bar{\tau}(z; z_o) = -\ln \left[\frac{\int_{E_m}^{E_M} E^{1-\alpha} e^{-\tau(E; z; z_o)} dE}{\int_{E_m}^{E_M} E^{1-\alpha} dE} \right] \quad (\text{A6})$$

Note that this is closely related to $\bar{D}_{pp}(z_o)$.

Finally, we will adopt the form of the physical density of TeV blazars, $\tilde{\phi}_B(L, z)$, described in the main text assuming a cutoff at $L_M = 2 \times 10^{46} \text{ erg s}^{-1}$, consistent with physical models of high-energy gamma ray blazars (see, e.g., Ghisellini et al. 2009). Associated with this we have a generalized number density,

$$\tilde{\Phi}_B(z; L_m, L_M) = \int_{\log_{10} L_m}^{\log_{10} L_M} \tilde{\phi}_B(z, L) d\log_{10} L \quad (\text{A7})$$

and luminosity density,

$$\tilde{\Lambda}_B(z; L_m, L_M) = \int_{\log_{10} L_m}^{\log_{10} L_M} L \tilde{\phi}_B(z, L) d\log_{10} L, \quad (\text{A8})$$

defined within a given intrinsic luminosity range.

A.2. Possible Definitions of \mathcal{N}_B

We now present various ways to define the number of high-energy gamma-ray blazars that are relevant for heating. These are compared in Figure 11, which supplements Figure 5 with additional approximations for \mathcal{N}_B .

A.2.1. Local number within a mean free path

Our first definition is the simplest one can imagine; choose an intrinsic luminosity range and use the local density to determine the number within a volume defined by the spectrally-average mean free path. That is,

$$\mathcal{N}_{B,I}(z_o; L_m) = \frac{4\pi}{3} \bar{D}_{pp}^3(z_o) \tilde{\Phi}_B(z_o; L_m, L_M). \quad (\text{A9})$$

This is an approximation of the number of sources with intrinsic luminosities in the specified range within an approximation of a single optical depth. This is shown for $L_m = 10^{45} \text{ erg s}^{-1}$ by the cyan dash-dotted line in Figure 11. Typically, where the

blazar population is rapidly evolving it tends to be a poor estimate of the number of sources, overestimating this number by nearly an order of magnitude at $z \gtrsim 3$.

A.2.2. Number within $\bar{\tau} = 1$

As long as $\tilde{\phi}_B(z, L)$ evolves slowly and $\bar{D}_{pp} \ll c/H_0$ it is unnecessary to perform the relevant redshift integral to get the volume element. However, this is not always the case, and thus a more accurate estimate is obtained by integrating the blazar number density within the volume specified by unit optical depth. That is,

$$\mathcal{N}_{B,II}(z_o; L_m) = \int_{z_o}^{z_1} 4\pi D_A^2(z; z_o) \frac{dD_P}{dz} \tilde{\Phi}_B(z; L_m, L_M) dz, \quad (\text{A10})$$

where z_1 is defined implicitly by $\bar{\tau}(z_1; z_o) = 1$.

For this definition, we may choose L_m in a variety of ways. In Figure 11 we show two in particular: that from setting $L_m = 10^{45} \text{ erg s}^{-1}$ (blue short-dashed line), which may be directly compared with the case shown for $\mathcal{N}_{B,I}$, and setting $L_m = L_{0.5}$ as defined by Equation (26), i.e., the luminosity-weighted median luminosity, above which sources produce half of the total local luminosity density (red dotted line). For $z \lesssim 3$ this approximation for \mathcal{N}_B gives similar results to $\mathcal{N}_{B,I}$ for a fixed L_m . At high redshifts, where $\tilde{\phi}_B$ is rapidly decreasing, the two diverge substantially. The difference between the $\mathcal{N}_{B,II}(z; L_{0.5})$ and the previous two is more striking, and a consequence for the assumed evolving luminosity distribution of blazars, which is clearly important.

A.2.3. Number of objects above a flux limit

While a fixed intrinsic luminosity limit may be useful conceptually, even idealized surveys do not directly probe such a population. Instead, most surveys are flux limited, and thus we also define a flux-limited definition of \mathcal{N}_B . In this case we set the minimum luminosity via

$$L_m(z; z_o, F_m) = 4\pi \left(\frac{1+z}{1+z_o} \right)^{\alpha-2} D_L^2(z; z_o) e^{\bar{\tau}(z; z_o)} F_m, \quad (\text{A11})$$

where F_m is a fixed flux limit, from which we obtain

$$\begin{aligned} \mathcal{N}_{B,III}(z_o; F_m) &= \int_{z_o}^{\infty} 4\pi D_A^2(z; z_o) \frac{dD_P}{dz} \\ &\quad \times \tilde{\Phi}_B[z; L_m(z; z_o, F_m), L_M] dz, \end{aligned} \quad (\text{A12})$$

This corresponds to the number of objects a flux-limited survey (in the 100 GeV–10 TeV band) performed by an observer at redshift z_o would detect. As such, it is the most directly comparable to the number of TeV blazars that have been observed. This is shown for flux limit comparable to that inferred for the TeV sample in Table 1, $4.19 \times 10^{-12} \text{ erg cm}^{-2} \text{ s}^{-1}$ in Figure 11 by the green long-dash-dotted line. Note that the number of objects found at $z = 0$ corresponds nicely to the number observed after correcting for incompleteness of present TeV surveys. Of course, this is by construction since $\tilde{\phi}_B$ was obtained from the observed population. Nevertheless, it is striking that many more objects would have been observed above this flux limit during earlier epochs, vastly exceeding any of the preceding approximations of \mathcal{N}_B . However, it does not necessarily follow that all of these sources will have contributed substantially to the heating rate.

A.2.4. Number of objects above a fractional heating rate imposed heating rate limit

The most relevant approximation for \mathcal{N}_B , and the one we adopt as our primary definition, is set by the heating rates directly. The general idea is to do what we do naturally at Earth: arrange all of the sources visible by an observer at z_o by the local heating rate they induce, from largest to smallest, and count until a fixed fraction of the total heating rate is reached. That is, set \mathcal{N}_B to be the minimum number of sources (on average) required to produce a given fraction of the total heating rate. Given its direct connection with the heating rate, this provides the most natural definition of the number of sources “responsible for the bulk of the heating.” To do this, however, we first must explicitly define the heating rate in terms of the appropriate functions.

Given a fixed spectrum, there is a linear relationship between the local flux and the heating rate, defined by Equation (9):

$$\begin{aligned} \dot{q} &= \int_{E_m}^{E_M} \frac{F_E e^{-\tau(E; z; z_o)}}{D_{pp} [E(1+z)/(1+z_o), z]} dE = \chi(z; z_o) F(E_m, E_M) \\ &= \chi(z; z_o) \left(\frac{1+z}{1+z_o} \right)^{2-\alpha} \frac{L}{4\pi D_L^2(z; z_o)}, \end{aligned} \quad (\text{A13})$$

where

$$\chi(z; z_o) \equiv \int_{E_m}^{E_M} \frac{E^{1-\alpha} e^{-\tau(E; z; z_o)}}{D_{pp} [E(1+z)/(1+z_o), z]} dE \Big/ \int_{E_m}^{E_M} E^{1-\alpha} dE, \quad (\text{A14})$$

is a function of the shape of the spectrum and the redshifts, similar to $\bar{\tau}(z; z_o)$. Thus, a given heating rate defines an intrinsic luminosity limit for a source at a given redshift:

$$L_m(z; z_o, \dot{q}_m) = 4\pi \left(\frac{1+z}{1+z_o} \right)^{\alpha-2} \frac{D_L^2(z; z_o)}{\chi(z; z_o)} \dot{q}_m. \quad (\text{A15})$$

With this, we may compute the heating rate as a function of \dot{q}_m , i.e., the heating rate associated with sources that produce a local heating larger than some limit:

$$\begin{aligned} \dot{Q}(z_o; \dot{q}_m) &= \int_{z_o}^{\infty} 4\pi D_A^2(z; z_o) \frac{dD_P}{dz} \\ &\quad \times \int_{\log_{10} L_m(z; z_o, \dot{q}_m)}^{\log_{10} L_M} \dot{q} \tilde{\phi}_B(z, L) d\log_{10} L dz \\ &= \int_{z_o}^{\infty} 4\pi D_A^2(z; z_o) \frac{dD_P}{dz} \left(\frac{1+z}{1+z_o} \right)^{2-\alpha} \\ &\quad \times \frac{\chi(z; z_o)}{4\pi D_L^2(z; z_o)} \tilde{\Lambda}_B [z; L_m(z; z_o, \dot{q}_m), L_M] dz. \end{aligned} \quad (\text{A16})$$

The heating from *all* gamma-ray blazars is obtained simply by setting $\dot{q}_m = 0$. On the other hand, we may set \dot{q}_m implicitly via

$$\dot{Q}(z_o; \dot{q}_m) = \mathcal{Q} \dot{Q}(z_o; 0), \quad (\text{A17})$$

where \mathcal{Q} ranges from 0 to 1, yielding a heating rate limit at each redshift that we shall call $\dot{q}_{\mathcal{Q}}$. From this, we may then obtain a number of contributing blazars:

$$\begin{aligned} \mathcal{N}_{B,IV}(z_o; \mathcal{Q}) &= \int_{z_o}^{\infty} 4\pi D_A^2(z; z_o) \frac{dD_P}{dz} \\ &\quad \times \tilde{\Phi}_B [z; L_m(z; z_o, \dot{q}_{\mathcal{Q}}), L_M] dz. \end{aligned} \quad (\text{A18})$$

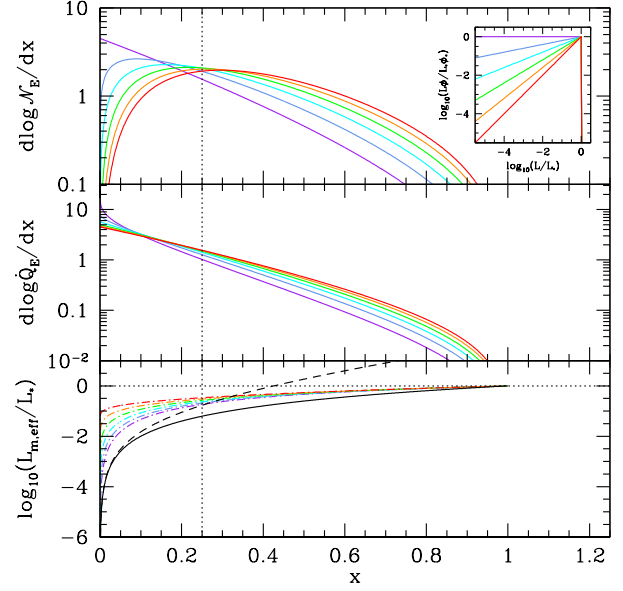


Figure 12. Radial distribution ($x \equiv D/D_*$) of the sources that contribute to the total number (top) and heating rate (middle), and the limiting and effective luminosity (bottom) for a flux-limited sample of sources described by a fixed, cutoff power-law luminosity function in a static Euclidean Universe. Different colors correspond to different luminosity function power-laws ($\xi = -1, -0.8, -0.6, -0.4, -0.2$, and 0 shown in violet, blue, cyan, green, orange, and red), with the associated luminosity-weighted luminosity function shown explicitly in the inset. For reference, the radius at which $D = D_{pp}$ is shown by the vertical dotted line. In comparison to the approximate L_m we used (black solid), we show the luminosity limit when absorption is included by the black dashed line, and the L_{eff} defined in Equation (A25) are shown by the dot-dash lines. This may be compared directly with Figure 14.

This is shown for $\mathcal{Q} = 0.5$ and $\mathcal{Q} = 0.75$ in Figure 11 by the black solid and long-dashed lines, respectively. While both are similar to the other measures of \mathcal{N}_B below $z \sim 1$, above this redshift they fall much more rapidly. This is due to the shift of $\tilde{\phi}_B(z, L)$ towards higher luminosities, and thus the luminosity density (and therefore heating rate) becomes dominated by fewer, more luminous sources. Nevertheless, \mathcal{N}_B is a rapidly increasing function of \mathcal{Q} , as evidence by the fact that $\mathcal{N}_{B,IV}$ increases by approximately an order of magnitude when \mathcal{Q} increases from 0.5 to 0.75.

A.3. Location and Properties of the Sources Responsible for the Bulk of the Heating

Armed with a definition of \mathcal{N}_B , we can now address which class of high-energy gamma-ray blazars dominates the heating rate. That is, we can assess whether the local heating is dominated by close, intrinsically dim objects or by distant, intrinsically luminous sources. This is done simply by inspecting the integrands in Equations (A16) and (A18). However, to interpret these, we will first build some intuition based upon an extremely simplified model, for which an analytical result is trivially obtained.

A.3.1. Static Euclidean Universe

We begin with a toy problem in which we consider a fixed power-law luminosity function in a static, Euclidean Universe. Specifically, we choose,

$$\tilde{\phi}(L) = \tilde{\phi}_* \left(\frac{L}{L_*} \right)^\xi \Theta \left(\frac{L_*}{L} \right), \quad (\text{A19})$$

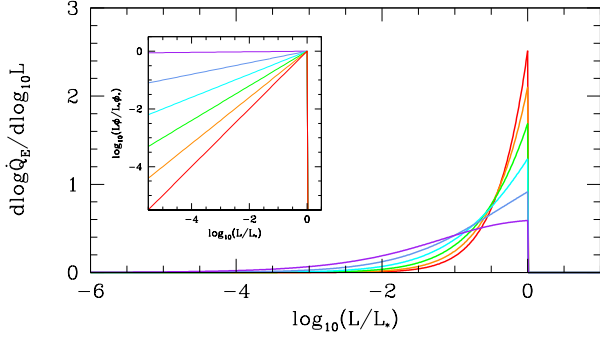


Figure 13. $d \log \dot{Q}_E / d \log_{10} L$ for a flux-limited sample of sources described by a fixed, cutoff power-law luminosity function in a static Euclidean Universe. Different colors correspond to different luminosity function power-laws, with the associated luminosity-weighted luminosity function shown explicitly in the inset. This may be compared directly with Figure 6.

where $\Theta(x)$ is the Heaviside function, $\tilde{\phi}_*$ is the overall normalization of the luminosity function, L_* is a maximum luminosity (approximating a break), and ξ is an arbitrary constant. We will also assume that D_{pp} is independent of energy, i.e., there is some characteristic value for which $\tau = D/D_{pp}$ and we may bring it out of the energy integral in the definition of \dot{q} . As a consequence, a fixed limit in \dot{q}_m corresponds directly to a fixed flux limit, F_m .

In a Euclidean Universe the number of objects takes the particularly simple form,

$$\begin{aligned} \mathcal{N}_E &= \int_0^\infty dD 4\pi D^2 e^{-D/D_{pp}} \int_{\log_{10} L_m}^\infty \tilde{\phi}(L) d\log_{10} L \\ &= \int_0^\infty dD 4\pi D^2 e^{-D/D_{pp}} \Theta\left(\frac{L_*}{L_m}\right) \\ &\quad \times \int_{\log_{10} L_m}^{\log_{10} L_*} \tilde{\phi}_* \left(\frac{L}{L_*}\right)^\xi d\log_{10} L. \end{aligned} \quad (\text{A20})$$

The flux limit, F_m , gives a luminosity limit of $L_m = 4\pi D^2 F_m$, where we have ignored the optical depth. Since we will be most concerned with how peaked the various integrands are at nearby distances, this is not a significant oversight (including it would serve to make them only more so). The definition of L_m implies a maximum distance as well, with $D_* = \sqrt{L_*/4\pi F_m}$, and therefore $L_m/L_* = (D/D_*)^2 \equiv x^2$. Thus, we have

$$\begin{aligned} \mathcal{N}_E &= \frac{4\pi \tilde{\phi}_*}{\ln 10} \int_0^{D_*} dD D^2 e^{-D/D_{pp}} \xi^{-1} \left[1 - \left(\frac{L_m}{L_*}\right)^\xi \right] \\ &= \frac{4\pi D_*^3 \tilde{\phi}_*}{\ln 10} \int_0^1 dx \xi^{-1} x^2 (1 - x^{2\xi}) e^{-x/x_{pp}}. \end{aligned} \quad (\text{A21})$$

From this we trivially obtain

$$\frac{d\mathcal{N}_E}{dD} = \frac{1}{D_*} \frac{d\mathcal{N}_E}{dx} = \frac{4\pi D_*^2 \tilde{\phi}_*}{\ln 10} \xi^{-1} x^2 (1 - x^{2\xi}) e^{-x/x_{pp}}, \quad (\text{A22})$$

providing some notion of the location of the most numerous sources. Typical values of ξ range from -1 to 0 , in practice, and $d \log \mathcal{N}_E / dx$ is shown in the top panel of Figure 12 for a variety of choices of ξ within this range.

The integral for \dot{Q} is similarly simple,

$$\begin{aligned} \dot{Q}_E &= \int_0^\infty dD 4\pi D^2 e^{-D/D_{pp}} \int_{\log_{10} L_m}^\infty \frac{L}{4\pi D^2 D_{pp}} \tilde{\phi}(L) d\log_{10} L \\ &= \frac{\tilde{\phi}_* L_* D_*}{\ln 10 D_{pp}} \int_0^1 dx \frac{1 - x^{2\xi+2}}{1 + \xi} e^{-x/x_{pp}}, \end{aligned} \quad (\text{A23})$$

and thus,

$$\frac{d\dot{Q}_E}{dD} = \frac{\tilde{\phi}_* L_*}{\ln 10 D_{pp}} \frac{1 - x^{2\xi+2}}{1 + \xi} e^{-x/x_{pp}}, \quad (\text{A24})$$

giving an idea of the location of the sources responsible for the bulk of the heating. For a variety of ξ , $d \log \dot{Q}_E / dx$ is shown in the middle panel of Figure 12.

Generally, we find that for all but the largest ξ , $d \log \mathcal{N}_E / dx$ and $d \log \dot{Q}_E / dx$ are peaked at small distances. In particular, both are typically dominated by $x < x_{pp}$. The bottom panel of Figure 12 shows the flux-limited L_m with (dashed) and without (solid) absorption included. Including absorption suppress the contributions at large x/x_{pp} , forcing $d \log \mathcal{N}_E / dx$ and $d \log \dot{Q}_E / dx$ to be even more strongly peaked at small distances.

Since L_m is a strong function of D , contributions from different distances have different luminosity distributions. It is possible to roughly characterize this by defining a typical luminosity, L_{eff} , associated with contributions at a given D :

$$L_{\text{eff}} \equiv 4\pi D^2 D_{pp} \frac{d\dot{Q}_E / dD}{d\mathcal{N}_E / dD} = L_* \frac{\xi}{1 + \xi} \frac{1 - x^{2\xi+2}}{1 - x^{2\xi}}. \quad (\text{A25})$$

With L_m , this is shown in the bottom panel of Figure 12. Generally L_{eff} is larger than L_m , and for small x substantially so. Thus, even for nearly flat $\tilde{\phi}(L)$ ($\xi \sim -1$) the objects that contribute to the heating are *not* dominated by the numerous, intrinsically dim objects with luminosities $L \sim L_m$.

Alternatively, we may perform the integral over D first, in which the flux limit implies a maximum distance to which a given object can be seen, $D_M = \sqrt{L/4\pi F_m}$, providing some insight into luminosity of the sources responsible for the heating. Doing so yields

$$\begin{aligned} \frac{d\dot{Q}_E}{d \log_{10} L} &= \frac{D_*}{D_{pp}} L \tilde{\phi}(L) \int_0^{D_M/D_*} e^{-x/x_{pp}} dx \\ &= \frac{D_*}{D_{pp}} L \tilde{\phi}(L) \left(1 - e^{-\sqrt{L/L_*}/x_{pp}} \right). \end{aligned} \quad (\text{A26})$$

This is shown in Figure 13 for a variety of ξ . In all cases the luminosity at the break in $\tilde{\phi}(L)$, i.e., L_* , contributes most significantly to the heating rate. However, the relative importance of lower-luminosity objects does depend upon the luminosity function; flat luminosity functions (i.e., $\xi = -1$) have many low-luminosity sources, and thus induce more broad $d \log \dot{Q}_E / d \log_{10} L$. Nevertheless, it appears that the heating rate in our simple toy model is generally dominated by nearby objects near the peak in the luminosity function.

A.3.2. TeV Blazars in the Standard Cosmology

We now return to the physically relevant case: heating due to TeV blazars with an evolving luminosity function in an evolving Universe. Here we specify the distributions of the sources responsible for producing a fraction Q of the total heating rate.

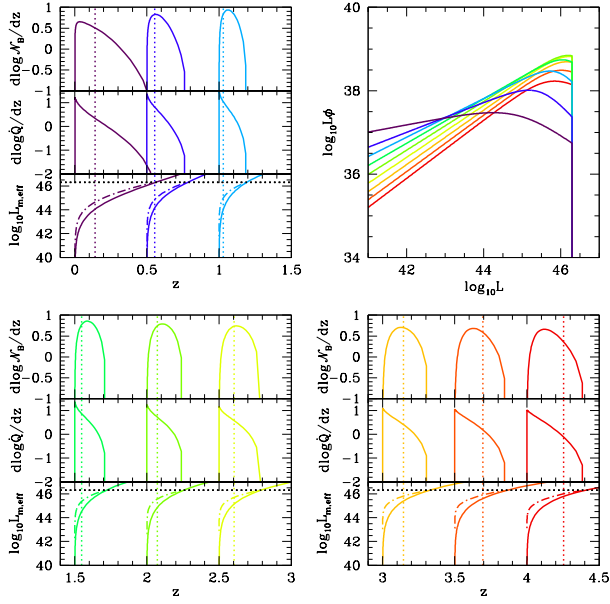


Figure 14. Redshift distribution of the sources that contribute to the total number (top-subpanel) and heating rate (middle-subpanel), and the limiting luminosity (bottom-subpanel) for a fractional \dot{Q} -limited sample of objects. Different colors correspond to different z_o , indicated by the left-most value of z for which each intersects the horizontal axis (z_o ranging from 0 to 4), and are consistent with those used in Figure 6. For reference, the redshifts at which $\bar{\tau}(z; z_o) = 1$ and L_m are shown by the vertical and horizontal dotted lines, respectively. In comparison to L_m , we also show L_{eff} (as defined by Equation (A28)) by the dash-dot lines. Finally, the upper-right panel shows $\phi_B(z_o, L)$ for each of the redshifts for which distributions are shown in the other panels, with corresponding colors (note that this shows the same relative dynamic range as that in the inset of Figures 12 and may thus be directly compared).

In this case, we may immediately read off dN_B/dz and $d\dot{Q}/dz$, the analogs of dN_E/dD and $d\dot{Q}_E/dD$, from Equations (A18) and (A16), respectively, yielding,

$$\begin{aligned} \frac{dN_B}{dz}(z; z_o) &= 4\pi D_A^2(z; z_o) \frac{dD_P}{dz} \tilde{\Phi}_B[z; L_m(z; z_o, \dot{q}_Q), L_m] \\ \frac{d\dot{Q}}{dz}(z; z_o) &= 4\pi D_A^2(z; z_o) \frac{dD_P}{dz} \left(\frac{1+z}{1+z_o} \right)^{2-\alpha} \\ &\quad \times \frac{\chi(z; z_o)}{4\pi D_L^2(z; z_o)} \tilde{\Lambda}_B[z; L_m(z; z_o, \dot{q}_Q), L_m]. \end{aligned} \quad (\text{A27})$$

These are shown, normalized by their integrated values, for z_o ranging from 0–4 in Figure 14 for $Q = 0.5$. In addition we show an analogously defined characteristic luminosity,

$$\begin{aligned} L_{\text{eff}}(z; z_o) &\equiv \frac{4\pi D_L^2(z; z_o)}{\chi(z; z_o)} \frac{d\dot{Q}/dz}{dN_B/dz} \\ &= \left(\frac{1+z}{1+z_o} \right)^{2-\alpha} \frac{\tilde{\Lambda}_B[z; L_m(z; z_o, \dot{q}_Q), L_m]}{\tilde{\Phi}_B[z; L_m(z; z_o, \dot{q}_Q), L_m]}. \end{aligned} \quad (\text{A28})$$

The generic features of our static toy model are also apparent here. At all observer redshifts the heating rate is dominated by the nearest sources. At low z_o , where $L\tilde{\phi}_B$ is nearly flat, the number of objects is also heavily weighted towards nearby objects, well within the redshift at which $\bar{\tau} = 1$. However, dN_B/dz and $d\dot{Q}/dz$ evolve with observer redshift due to both, the intrinsic evolution of $\tilde{\phi}_B$ and the background Universe. As a consequence, by $z_o \sim 0.5$ the peak of dN_B/dz has moved to the $\bar{\tau} = 1$

redshift, implying that z_1 (where $\bar{\tau}(z_1, z_o) = 1$) is not a particularly accurate estimate of the redshifts that contribute significantly to the heating. This is further supported by the high- z_o behavior of dN_B/dz , which once again is heavily weighted at redshifts inside of z_1 due to onset of the decline in the blazar population.

The typical luminosities of objects responsible for the heating also evolve. At $z_o \sim 0$ these are roughly $10^{44} \text{ erg s}^{-1}$, rising to $3 \times 10^{45} \text{ erg s}^{-1}$ by $z_o \sim 2$. We also compute the heating rate per logarithmic decade in luminosity:

$$\begin{aligned} \frac{d\dot{Q}}{d\log_{10} L} &= \int_{z_o}^{z_m} 4\pi D_A^2(z; z_o) \frac{dD_P}{dz} \left(\frac{1+z}{1+z_o} \right)^{2-\alpha} \\ &\quad \times \frac{\chi(z; z_o)}{4\pi D_L^2(z; z_o)} L \tilde{\phi}_B(z, L), \end{aligned} \quad (\text{A29})$$

(where z_m is determined implicitly by $L_m(z_m; z_o, \dot{q}_Q) = L$) shown in Figure 6 for a number of z_o . At $z_o \sim 0$ the distribution of heating rates is a relatively broad function of L centered near 10^{45} ergs . Until $z_o \sim 2$, as z_o grows $d\dot{Q}/d\log_{10} L$ becomes increasingly peaked and centered upon increasingly larger luminosities. Above $z_o \sim 2$ this trend reverses, though the distribution of luminosities that contribute appreciably to the heating rate never becomes comparable to that in the present epoch. Thus, generally it appears that the heating is due predominantly to nearby objects with luminosities comparable to $10^{45} \text{ erg s}^{-1}$.

REFERENCES

- Abdo, A. A., et al. 2009a, *ApJ*, 700, 597
- . 2009b, *ApJ*, 706, L138
- . 2009c, *ApJ*, 707, 580
- . 2009d, *Science*, 323, 1688
- . 2010a, *ApJ*, 715, 429
- . 2010b, *ApJ*, 716, 30
- Acciari, V., et al. 2009a, *ApJ*, 690, L126
- Acciari, V. A., et al. 2008, *ApJ*, 679, 397
- . 2009b, *ApJ*, 707, 612
- . 2009c, *ApJ*, 693, L104
- . 2010a, *ApJ*, 709, L163
- . 2010b, *ApJ*, 708, L100
- . 2010c, *ApJ*, 715, L49
- Acero, F., et al. 2009, *Science*, 326, 1080
- Ackermann, M., et al. 2010, *ApJ*, 717, L127
- . 2011, *ApJ*, 729, 114
- Aharonian, F., et al. 2002, *A&A*, 384, L23
- . 2003, *A&A*, 406, L9
- . 2005, *A&A*, 436, L17
- . 2006a, *Nature*, 440, 1018
- . 2006b, *A&A*, 455, 461
- . 2007a, *A&A*, 470, 475
- . 2007b, *A&A*, 473, L25
- . 2007c, *A&A*, 475, L9
- . 2008a, *A&A*, 481, L103
- . 2008b, *A&A*, 477, 481
- . 2010, *A&A*, 521, 69
- Albert, J., et al. 2006, *ApJ*, 648, L105
- . 2007a, *ApJ*, 666, L17
- . 2007b, *ApJ*, 667, L21
- . 2007c, *ApJ*, 662, 892
- Aleksić, J., et al. 2010, *ApJ*, 723, L207
- Aliu, E., et al. 2009, *ApJ*, 692, L29
- Atkins, R., et al. 2000, *ApJ*, 533, L119
- . 2003, *ApJ*, 583, 824
- Bartlett, J. G., & Stebbins, A. 1991, *ApJ*, 371, 8
- Becker, G. D., Rauch, M., & Sargent, W. L. W. 2007, *ApJ*, 662, 72
- Bersanelli, M., Bensadoun, M., de Amici, G., Levin, S., Limon, M., Smoot, G. F., & Vinje, W. 1994, *ApJ*, 424, 517
- Bolton, J. S., & Becker, G. D. 2009, *MNRAS*, 398, L26

- Bolton, J. S., Haehnelt, M. G., Viel, M., & Springel, V. 2005, *MNRAS*, 357, 1178
- Bolton, J. S., Viel, M., Kim, T., Haehnelt, M. G., & Carswell, R. F. 2008, *MNRAS*, 386, 1131
- Bret, A., Firpo, M., & Deutsch, C. 2004, *Phys. Rev. E*, 70, 046401
- . 2005, *Physical Review Letters*, 94, 115002
- Bret, A., Gremillet, L., & Bénisti, D. 2010a, *Phys. Rev. E*, 81, 036402
- Bret, A., Gremillet, L., & Dieckmann, M. E. 2010b, *Physics of Plasmas*, 17, 120501
- Broderick, A. E., Chang, P., & Pfrommer, C. 2012, *ApJ* in print, arXiv:1106.5494
- Caputi, K. I., et al. 2007, *ApJ*, 660, 97
- Chandra, P., et al. 2010, *Journal of Physics G Nuclear Physics*, 37, 125201
- Cooray, A., & Furlanetto, S. R. 2004, *ApJ*, 606, L5
- Davé, R., Oppenheimer, B. D., Katz, N., Kollmeier, J. A., & Weinberg, D. H. 2010, *MNRAS*, 408, 2051
- de Cea del Pozo, E., Torres, D. F., & Rodríguez Marrero, A. Y. 2009, *ApJ*, 698, 1054
- Dermer, C. D., Cavadini, M., Razzaque, S., Finke, J. D., Chiang, J., & Lott, B. 2011, *ApJ*, 733, L21
- Dermer, C. D., & Schlickeiser, R. 2002, *ApJ*, 575, 667
- Dolag, K., Kachelriess, M., Ostapchenko, S., & Tomàs, R. 2011, *ApJ*, 727, L4
- Domingo-Santamaría, E., & Torres, D. F. 2005, *A&A*, 444, 403
- Doroshkevich, A. G. 1970, *Astrophysics*, 6, 320
- Faucher-Giguère, C., Lidz, A., Hernquist, L., & Zaldarriaga, M. 2008, *ApJ*, 682, L9
- Faucher-Giguère, C., Lidz, A., Zaldarriaga, M., & Hernquist, L. 2009, *ApJ*, 703, 1416
- Fixsen, D. J., Cheng, E. S., Gales, J. M., Mather, J. C., Shafer, R. A., & Wright, E. L. 1996, *ApJ*, 473, 576
- Fixsen, D. J., & Mather, J. C. 2002, *ApJ*, 581, 817
- Franceschini, A., Rodighiero, G., & Vaccari, M. 2008, *A&A*, 487, 837
- Fukugita, M., & Peebles, P. J. E. 2004, *ApJ*, 616, 643
- Furlanetto, S. R., & Oh, S. P. 2008, *ApJ*, 682, 14
- Gehrels, N., Ramírez-Ruiz, E., & Fox, D. B. 2009, *ARA&A*, 47, 567
- Ghisellini, G., & Maraschi, L. 1989, *ApJ*, 340, 181
- Ghisellini, G., Maraschi, L., & Tavecchio, F. 2009, *MNRAS*, 396, L105
- Ghisellini, G., & Tavecchio, F. 2008, *MNRAS*, 387, 1669
- Goto, T., et al. 2010, *A&A*, 514, 6
- Gould, R. J., & Schröder, G. P. 1967, *Physical Review*, 155, 1408
- HESS Collaboration et al. 2010, *A&A*, 520, 83
- Hopkins, P. F., Richards, G. T., & Hernquist, L. 2007, *ApJ*, 654, 731
- Huang, D., Konopelko, A., & for the VERITAS collaboration. 2009, arXiv:0912.3772
- Hui, L., & Gnedin, N. Y. 1997, *MNRAS*, 292, 27
- Hui, L., & Haiman, Z. 2003, *ApJ*, 596, 9
- Inoue, Y., & Totani, T. 2009, *ApJ*, 702, 523
- Jones, T. W., O'dell, S. L., & Stein, W. A. 1974, *ApJ*, 192, 261
- Kennicutt, Jr., R. C. 1998, *ARA&A*, 36, 189
- Kneiske, T. M., Bretz, T., Mannheim, K., & Hartmann, D. H. 2004, *A&A*, 413, 807
- Kneiske, T. M., & Mannheim, K. 2008, *A&A*, 479, 41
- Komatsu, E., et al. 2011, *ApJS*, 192, 18
- Kravtsov, A. 2010, *Advances in Astronomy*, 2010
- Lacki, B. C., Thompson, T. A., Quataert, E., Loeb, A., & Waxman, E. 2010, arXiv: 1003.3257
- Le Floc'h, E., et al. 2005, *ApJ*, 632, 169
- Lidz, A., Faucher-Giguère, C., Dall'Aglio, A., McQuinn, M., Fechner, C., Zaldarriaga, M., Hernquist, L., & Dutta, S. 2010, *ApJ*, 718, 199
- MAGIC Collaboration et al. 2008, *Science*, 320, 1752
- Magnelli, B., Elbaz, D., Chary, R. R., Dickinson, M., Le Borgne, D., Frayer, D. T., & Willmer, C. N. A. 2009, *A&A*, 496, 57
- McQuinn, M., Lidz, A., Zaldarriaga, M., Hernquist, L., Hopkins, P. F., Dutta, S., & Faucher-Giguère, C. 2009, *ApJ*, 694, 842
- Narumoto, T., & Totani, T. 2006, *ApJ*, 643, 81
- Neronov, A., & Semikoz, D. V. 2009, *Phys. Rev. D*, 80, 123012
- Neronov, A., & Vovk, I. 2010, *Science*, 328, 73
- Oh, S. P. 1999, *ApJ*, 527, 16
- Paglionie, T. A. D., Marscher, A. P., Jackson, J. M., & Bertsch, D. L. 1996, *ApJ*, 460, 295
- Peebles, P. J. E. 1980, *The large-scale structure of the universe*, ed. Peebles, P. J. E.
- . 2001, *ApJ*, 557, 495
- Penton, S. V., Shull, J. M., & Stocke, J. T. 2000a, *ApJ*, 544, 150
- Penton, S. V., Stocke, J. T., & Shull, J. M. 2000b, *ApJS*, 130, 121
- . 2002, *ApJ*, 565, 720
- . 2004, *ApJS*, 152, 29
- Persic, M., Rephaeli, Y., & Arieli, Y. 2008, *A&A*, 486, 143
- Pfrommer, C., Chang, P., & Broderick, A. E. 2012, *ApJ* in print, arXiv:1106.5505
- Piran, T. 2004, *Reviews of Modern Physics*, 76, 1143
- Ponente, P. P., Diego, J. M., Sheth, R. K., Burigana, C., Knollmann, S. R., & Ascasibar, Y. 2011, *MNRAS*, 410, 2353
- Puchwein, E., Pfrommer, C., Springel, V., Broderick, A. E., & Chang, P. 2011, arXiv:1107.3837
- Raue, M., et al. 2010, in *Astronomical Society of the Pacific Conference Series*, Vol. 427, *Astronomical Society of the Pacific Conference Series*, ed. L. Maraschi, G. Ghisellini, R. Della Ceca, & F. Tavecchio, 302
- Reisenegger, A., & Miralda-Escudé, J. 1995, *ApJ*, 449, 476
- Rephaeli, Y., Arieli, Y., & Persic, M. 2010, *MNRAS*, 401, 473
- Salamon, M. H., & Stecker, F. W. 1998, *ApJ*, 493, 547
- Sikora, M., Begelman, M. C., & Rees, M. J. 1994, *ApJ*, 421, 153
- Soltan, A. 1982, *MNRAS*, 200, 115
- Springel, V., White, M., & Hernquist, L. 2001, *ApJ*, 549, 681
- Takahashi, K., Mori, M., Ichiki, K., & Inoue, S. 2012, *ApJ*, 744, L7
- Tavecchio, F., & Ghisellini, G. 2008, *MNRAS*, 386, 945
- Tavecchio, F., Ghisellini, G., Bonnoli, G., & Foschini, L. 2011, *MNRAS*, 414, 3566
- Tavecchio, F., Ghisellini, G., Foschini, L., Bonnoli, G., Ghirlanda, G., & Coppi, P. 2010, *MNRAS*, 406, L70
- Taylor, A. M., Vovk, I., & Neronov, A. 2011, *A&A*, 529, A144
- Thompson, T. A., Quataert, E., & Waxman, E. 2007, *ApJ*, 654, 219
- Venters, T. M. 2010, *ApJ*, 710, 1530
- VERITAS Collaboration et al. 2009, *Nature*, 462, 770
- Viel, M., Bolton, J. S., & Haehnelt, M. G. 2009, *MNRAS*, 399, L39
- Vovk, I., Taylor, A. M., Semikoz, D., & Neronov, A. 2012, *ApJ*, 747, L14